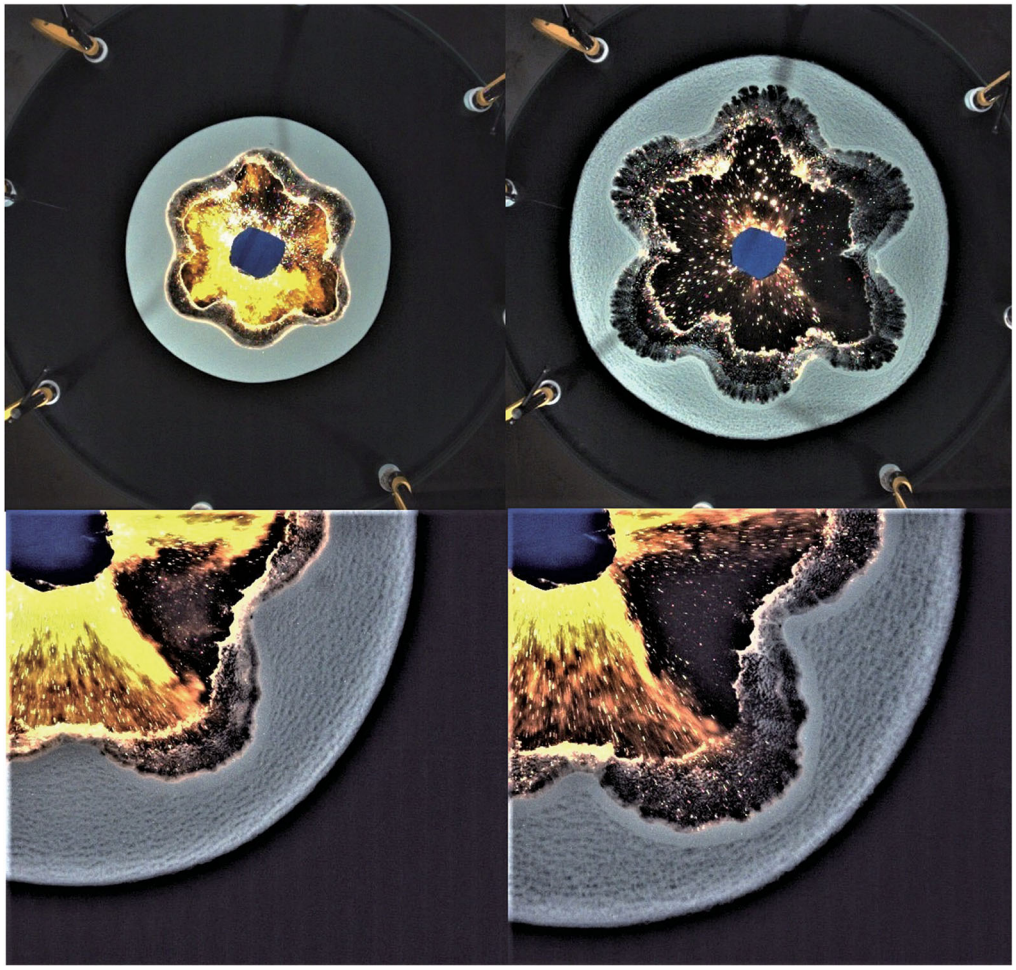

Showcasing experiments from the State Key Laboratory of Explosive Science and Technology, the Beijing Institute of Technology, from the group of Dr Kun Xue.

Morphodynamics of a dense particulate medium under radial explosion

Hierarchical structures are observed in the destabilized interfaces of granular media impacted by blast waves. Analogous to the classic hydrodynamic RM instability, the shock loaded surface of granular media will also develop into a signature spike-bubble structure despite of distinct underlying physics. Xue *et al.* characterize the spatiotemporal evolution of a hierarchical pattern arising from the blast loaded surfaces of granular media which is found to be related to the heterogeneous granular flows as a result of shock interaction.

As featured in:

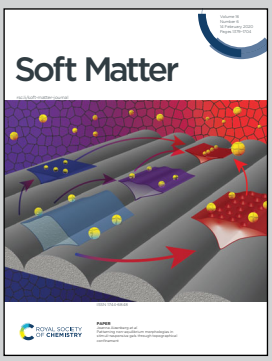

See Kun Xue *et al.*, *Soft Matter*, 2020, **16**, 1498.

ROYAL SOCIETY OF CHEMISTRY

rsc.li/soft-matter-journal

Registered charity number: 207890

Soft Matter

PAPER

View Article Online
View Journal | View Issue

Check for updates

Cite this: *Soft Matter*, 2020, **16**, 1498

Morphodynamics of a dense particulate medium under radial explosion

Kun Xue,*[a] Panpan Han,[a] Kaiyuan Du,[a] Yixiang Gan,[b] Ziwei Wang[a] and Chunhua Bai[a]

In this paper, we investigate the initiation and growth of instability patterns arising from the shock loaded internal surfaces of granular rings confined in a Hele-Shaw cell using both experimental and numerical approaches. A variety of patterns are formed in granular media consisting of grains with varying morphologies. When the particle shape becomes increasingly irregular, and/or the gap in the Hele-Shaw cell becomes narrower, it is increasingly hard for confined particles to fluidize. Consequently the emergent pattern transitions from a smooth circle with trivial undulation which grows in a self-similar manner to an unstable finger-like structure with significant tip-splitting. The distinct growth mode of the well-defined instability pattern is closely associated with its inception phase alongside the transmission of the compaction front. The runaway growth of the incipient perturbations gives rise to the unstable growth of the late-time finger-like instabilities. Conversely the minimal growth of the perturbations in the inception phase guarantees the ensuing self-similar growth of the instability patterns featuring insignificant corrugation. The grain-scale simulations reveal the fundamental role played by the heterogeneous non-linear force network inherent to granular media in the stable-to-unstable transition of the instability pattern. The present work reveals the correlation between the grain-scale physics underpinning the formation of surface instability upon shock loading granular media and the nature of the resulting macro-scale instability patterns. The macroscopic flowability of particles through the confined space is found to be the foremost indicator of the nature of the shock induced granular instability pattern.

Received 29th October 2019,
Accepted 15th December 2019

DOI: 10.1039/c9sm02150g

rsc.li/soft-matter-journal

Published on 18 December 2019. Downloaded on 2/14/2020 10:45:36 AM.

I Introduction

The interaction of shocks/blasts with granular media interfaces is not only of fundamental scientific interest but also relevant to natural phenomena and engineering processes,[1] such as volcanic eruptions,[2] explosions of supernovas,[3] laser-driven inertial confinement fusion experiments,[4] and the accidental explosion of combustible dust–air mixtures or hybrid systems containing powder and combustible gases, which is a concern in the loss prevention industry.[5] A granular medium subjected to impulsive loading does not expand homogeneously. Instead, jet-like structures are formed all around the particle cloud front as a result of finger-like patterns arising from the shock destabilized interface.[1,6–14]

Studies focusing on the shock/blast waves propagating into particle laden gases with the solid fraction barely exceeding 1% attribute the fingering in such particulate systems to the hydrodynamic Ritchmyer–Meshkov (RM) instability.[15–18] Whereas the growth rates of the particulate jets formed during explosive dispersal of dense dry/wet particle packs or suspensions are found to be significantly larger than those of the classical gas-dynamic Rayleigh–Taylor (RT)/RM instabilities.[19,20] Actually it is quite debatable whether a shock compacted particulate system could be modeled as an analogue fluid system since the heterogeneity arising from the grain-scale processes dominates the shock compaction dynamics of particles.[21,22]

The lack of thorough understanding of the nature of the fingering pattern in shock loaded granular media is largely due to the complex momentum and energy transmission in granular media involving the shock interaction with particles, the interaction between particles and the interaction between gases and particles.[23,24] The gas–particle coupling through the pore pressure gradient governed by Darcy's law is found to be responsible for the extension of "gas fingers" in a dense particle pack which is invaded by slowly injected gases, or particles falling into air driven by gravity.[25–29] Whereas the timescale associated with pressure diffusion in particle packs is much longer than that those associated with the shock interaction and inter-particle interaction. Furthermore the shock loads suffice to compact the particle packs to the maximum random packing density or even higher, whereby the pressure diffusion is significantly slowed. Thus the pore pressure gradients

[a] State Key Laboratory of Explosive Science and Technology, Beijing Institute of Technology, Beijing, 100081, China. E-mail: xuekun@bit.edu.cn
[b] School of Civil Engineering, The University of Sydney, Sydney, Australia

This journal is © The Royal Society of Chemistry 2020

Published on 18 December 2019. Downloaded on 2/14/2020 10:45:36 AM.

and the drag forces ought to be secondary controlling factors which contribute more to the evolution of the instability pattern at late times than the initiation of instabilities. Actually without taking into account the pressure diffusion and drag forces, Kandan *et al.* successfully reproduce the initiation of surface instabilities in the continuum modeling of shock loaded one-dimensional particle columns in which the corrugated surface is subjected to ramped-up pressure.[14] One issue with their continuum approach is that the Drucker–Prager solid model used in the continuum simulations considerably underestimates the energy dissipation due to the inelastic collisions and friction between particles. Besides, the continuum modeling of granular media ignores the highly heterogeneous transmission of stresses intrinsic to the granular media. The stresses in granular media can only be transmitted through columns of particles, known as force chains, which collectively form an intricate network.[30–32] The distinctive force structure in granular systems is strongly dependent on the geometry, loading conditions and packing structures, and is found to be responsible for various granular flows and bulk-scale stress–strain relations.[21,22,31,32] In the pursuit of fundamental physical understanding of the mechanisms underlying the instability pattern in shock loaded granular media, it is necessary to elucidate the decisive role played by the distinct force structures sustained by the shock loading.

In this work, we first carry out experiments based on a radial Hele-Shaw cell to investigate the instability pattern formed by a granular interface impinged by a divergently propagating shock front. The instability patterns are found to dramatically change with the particle morphology (shape and roughness) as well as with the gap size of the Hele-Shaw cell. More importantly the instability pattern can change from a stable pattern governed by the proportionate growth mode to an unstable branched fingering pattern. Numerical simulations based on the discrete element method (DEM) are performed to identify the grain-scale physics underpinning the stable-to-unstable transition of the granular instability pattern. Special attention is focused on the relationship between the particle morphology/boundary effect, grain-scale heterogeneous force structures, meso-scale particle flows, and macroscopic pattern transition.

II Methods

A Experimental setup

In order to exert a divergent shock load onto the internal surface of a semi-two-dimensional particle ring, we devised an experimental system consisting of a radial Hele-Shaw cell fitted with a large pressurized tank beneath as schematized in Fig. 1(a). The 20 mm diameter exit of the pressurized tank is aligned with the central orifice with the same diameter in the bottom plate of the Hele-Shaw cell. The top and bottom Plexiglass plates (600 × 600 × 20 mm) of the Hele-Shaw cell are separated by 4 or 2 mm spacers and clamped together around the edge. A concentric particle ring with inner and outer diameters of 20 and 500 mm is disposed around the bottom orifice and confined inside the Hele-Shaw cell. No gap is discernable between the top surface of the particle ring and the top plate. The internal and external surfaces of the particle ring are free of casings.

Since the characteristic time associated with the pattern formation is on the order of milliseconds, the ramp time of the shock loading should be at least less than 1 ms, entailing a similar short opening time of the orifice. A double chamber apparatus with a vertical plunger valve is devised to serve as the fast opening valve for the high-pressure tank as shown in Fig. 1(a). A 20 mm diameter plunger goes through the upper chamber and connects a piston separating the upper and bottom chambers. The pressure in the upper chamber, p_{up}, is initially slightly lower than that in the bottom one, p_{bo}, $p_{up} < p_{bo}$, so that the jacked up plunger tightly plugs the exit of the pressurized chamber. Once the gas in the bottom chamber is evacuated, the pressure differential between the upper and

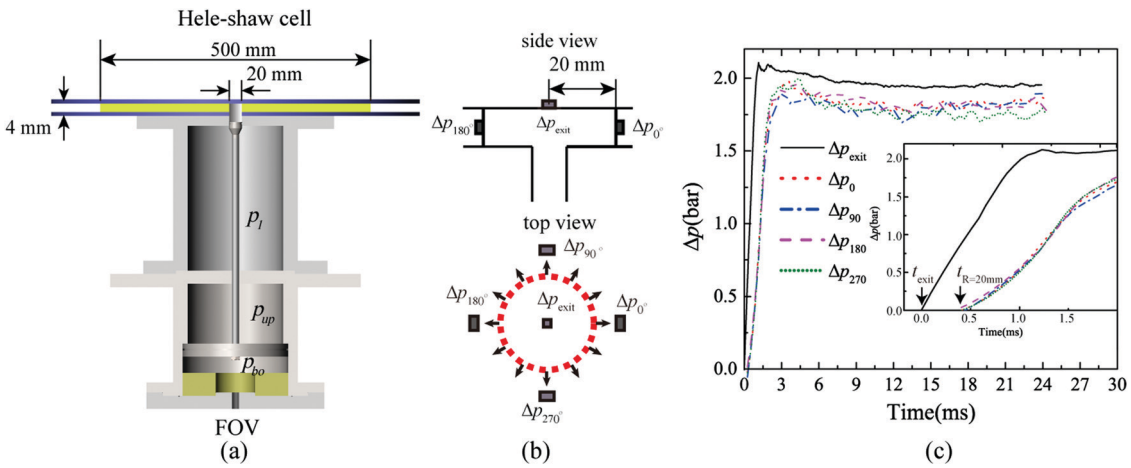

Fig. 1 (a) Schematic of the experimental setup consisting of a top Hele-Shaw cell, a middle pressurized tank and a bottom double-chambered fast opening valve (FOV). (b) Side view (top panel) and top view (bottom panel) of the pressure transducer arrangement. (c) Overpressure histories recorded by transducers installed in the manner shown in (b).

Published on 18 December 2019. Downloaded on 2/14/2020 10:45:36 AM.

bottom chambers immediately pulls down the plunger, with pressurized gas bursting into the gaps between the top and bottom plates of the Hele-Shaw cell. The radial expansion of the pressurized gas released from the pressurized tank issues an outgoing cylindrical incident shock wave into the particle ring.

The pressure evolutions at positions above the bottom orifice (Δp_{exit}) and inside the Hele-Shaw cell with a short distance from the exit (Δp_0, Δp_{90}, Δp_{180}, and Δp_{270}) are recorded by Kistler pressure transducers therein. The arrangement of the transducers and the corresponding overpressure curves are presented in Fig. 1(b) and (c), respectively. All overpressure profiles exhibit similar shapes, specifically an impulsive pressure jump with a ramp time less than 0.7 ms followed by a plateau with a duration of dozens of milliseconds. Note that the pressure signals inside the Hele-Shaw cell which are obtained at positions with the same radii but different azimuthal angles can fairly collapse into one curve, indicating a homogeneous divergent flow. The shock waves generated by the apparatus described above show good repeatability in terms of the recorded pressure signals. Varying the pressure in the pressurized tank can change the peak overpressure of the shock loads, Δp_{max}. Δp_{max} investigated in the present work ranges from 1 to 5 bar. From the time interval between the arrival times in the pressure signals at different radii, we can deduce the Mach number of the incident wave, which is found to range from 1.07 to 1.48.

The morphodynamics of dense particle rings whose internal surfaces are impinged by the outgoing cylindrical shock waves are recorded by a high-speed camera (Photron SA-X) placed above the Hele-Shaw cell with a frame rate of 20 000 f s^{-1}, exposure time 1/50 000 s and a spatial resolution of 1024 × 1024, or 290 μm per pixel.

B Material characterization

Five different particulate materials are tested: smooth spherical glass beads, smooth PMMA spheres, angular polystyrene particles, and two types of rough quartz sand (Sand #1 and #2). The macroscopic packing fraction and the packing microstructure both are sensitive to the size distribution and the morphology of the particles. Fig. 2 presents the respective size distribution curves in terms of density (q_3) and cumulative distributions (Q_3) by volume for the five samples. Table 1 summarizes the statistical characteristics of the particle size distributions, such as the average particle size (D_{50}), the polydispersity (δ), which measures the spread of the distribution, and the shape skewness (S). δ and S are calculated by eqn (1) and (2) respectively,

$$\delta = \sqrt{\langle \Delta d_p^2 \rangle} \Big/ \langle d_p \rangle \quad (1)$$

$$S = \sqrt{\langle \Delta d_p^3 \rangle} \Big/ \langle \Delta d_p^3 \rangle^{\frac{3}{2}} \quad (2)$$

Here, d_p is the particle diameter, $\Delta d_p = d_p - \langle d_p \rangle$ and the moments of d_p (and Δd_p) are defined as $\left\langle d_p^n \right\rangle = \int d_p^n P(d_p) d(d_p)$ (and $\left\langle \Delta d_p^n \right\rangle = \int \Delta d_p^n P(d_p) d(d_p)$).

Although the tested particles change moderately in terms of particle size distribution (see Table 1), the particle shape drastically changes from almost spherical (glass and PMMA spheres) to highly angular (TPU and quartz sand grains) as

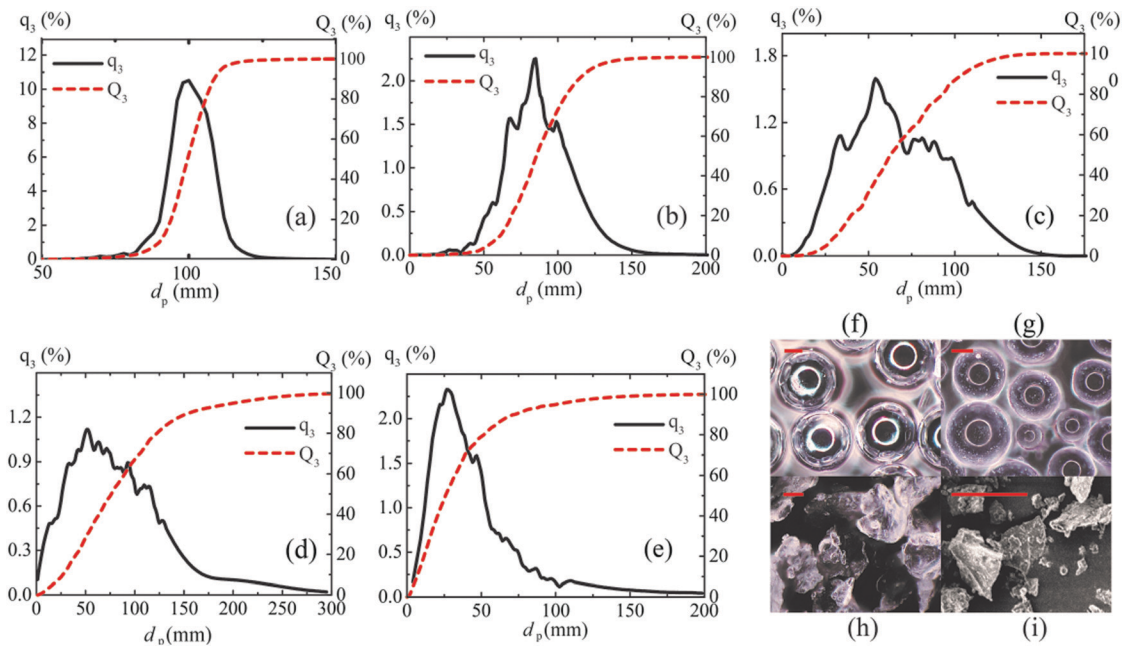

Fig. 2 (a–e) Density and cumulative distributions, q_3 and Q_3, of the particle diameters, d_p, for glass beads (a), PMMA spheres (b), TPU particles (c), and Sand #1 (d) and #2 (e) grains. (f–i) High resolution optical microscopic images of glass beads (f), PMMA spheres (g), TPU particles (h), and Sand #2 grains (i). The length scales in (f–i) represent 30 μm.

 This journal is © The Royal Society of Chemistry 2020

Published on 18 December 2019. Downloaded on 2/14/2020 10:45:36 AM.

Table 1 Physical properties and dynamic flowability measurements of the samples. D_{50}: the average particle size, δ: polydispersity, S: skewness of the particle size distribution; ρ: material density; ϕ: packing fraction of the particle ring; FE_{comp}: flow energy of the compacted sample; Φ_p: inter-particle friction angle; Φ_{wall}: wall–particle friction angle

	Glass	PMMA	TPU	Sand #1	Sand #2
D_{50}	98.3	86.4	57.7	64.0	34.8
δ	0.0939	0.2525	0.4175	0.63	0.8688
S	1.0732	0.4060	0.3420	1.1763	1.8814
ρ (g cm^{-3})	2.5	1.19	1.18	2.65	2.65
Sphericity	0.92	0.94	0.768	0.664	0.688
ϕ	0.6	0.6	0.39	0.51	0.36
Compressibility	2.7	3.24	24	4.39	21.79
FE_{comp} (mJ)	160	140	1152	1091	1645
Φ_p	16.9	18.3	34.35	36.2	45.3
Φ_{wall}	8.84	10.33	18.5	29.77	36.1

shown in the images (see Fig. 2(f–i)) obtained from the high-resolution stereoscopic optical microscope. The sphericities of grains (S_p) for all samples measured by the projection sphericity and the inscribed circle sphericity (see Table 1) quantify the irregularities of the particle shapes, again substantiating what is discerned from the microscopic images.

The particle morphology and size distribution also strongly influence the macroscopic properties of particle packs, such as flowability, compressibility, friction angle, *etc.*, which are pertinent to granular flows.[33,34] A range of macroscopic properties of particles are measured by a Freeman FT4 powder rheometer, including compressibility, shear strength (inter-particle friction angle, Φ_p), the flow energy of the compacted particles (FE_{comp}) and the angle of wall friction (Φ_{wall}) as presented in Table 1. More details about the measurement methodologies can be found in ref. 35. In the present study the particles have to move through the narrow gap inside the Hele-Shaw cell; the boundary effects as a function of the wall–particle friction and the pressure thus play an integral part in the flowability of the particles.

The particle packings consisting of strongly angular grains (TPU and sand grains) are looser than those formed by spherical beads and have larger compressibility. The flow energy and shear strength of the compacted powders both correlate with the sphericity of the powders since the interlocking of angular particles substantially increases the shear resistance of powders.[34] It is worth noting that the TPU sample exhibits much smaller wall friction compared with the two types of sand with similar sphericity, which is probably thanks to the smoother corners and edges of TPU particles.

C Numerical method

The numerical investigations are performed using a discrete element method (DEM) code LIGGGHTS.[36] The DEM is a numerical scheme that has been successfully used to simulate the response of granular media by modeling the dynamic behavior of large assemblies of circular disks, spheres, and blocks.[37,38] LIGGGHTS solves Newton's second law of motion and force–displacement laws at the contact using an explicit finite difference method. A Hertz–Mindlin contact model, a variant of the non-linear spring–dashpot contact model based on Hertz–Mindlin contact theory, is assumed in this study. Since the morphology of the particles employed in the experiments varies greatly, especially the particle shape, it is necessary to properly take into account the particle shape effect in the simulations. Currently, the suitable modeling methodology of shape effects by DEM can be classified into two major approaches: (1) introducing artificial rolling resistance at contacts between disks or spheres to partially restrict the relative rotations between grains, and (2) generating realistic particle shapes by using irregular geometries.[33] Although the second approach can better reproduce the shape effects including the rolling resistance and inter-locking, it is numerically prohibited for the systems consisting of millions of particles investigated in the present work. Instead we adopt the first approach due to its efficiency and simplicity.[33,39] Moreover the inter-locking between irregular particles is mimicked by increasing the inter-particle friction coefficient.[34] The present DEM simulations are aimed at elucidating the role played by the particle morphology in the pattern formation in shock loaded granular media rather than quantifying the dependence of the pattern structure on the particle morphology. To this end, it suffices to

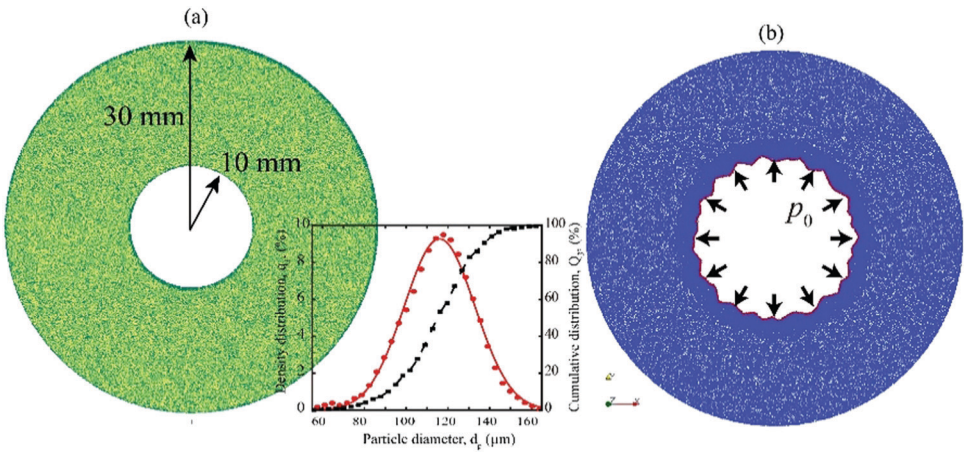

Fig. 3 Snapshots of simulated particle rings before (a) and during (b) the shock loading. Inset: The diameter distribution of particles. The shades of the particles in (a) correspond to the particle diameters. The innermost layer of particles shaded in red in (b) is those subjected to the impulsive loads.

Published on 18 December 2019. Downloaded on 2/14/2020 10:45:36 AM.

differentiate the angular grains from spherical ones using a combination of an elevated friction coefficient and rolling resistance coefficient. Details of the contact model, the rolling resistance model and the parameters used in the simulations are presented in Appendix A.

The particle packing is established by first letting free-falling spherical particles settle by gravity in short annular simulation boxes with inner and outer diameters of 20 and 60 mm, respectively, and allowing them to relax until the kinetic energy of the assembly ceases to decrease. The particle size distribution follows a Gaussian function with D_{50} = 114 μm and δ = 28 μm (see the inset in Fig. 3(a)). The particle ring generated in this manner consists of about two layers of particles across the height of the ring, enabling significant boundary effects. Therefore the particle morphology and boundary effects both make pivotal contributions to the flowability of the particles, eventually influencing the granular flows in the Hele-Shaw cell. Four sets of particle–wall combinations are to be examined, namely rough particles/rough boundaries, rough particles/smooth boundaries, smooth particles/rough boundaries, and smooth particles/smooth boundaries. Note that rough particles invoke an elevated inter-particle friction coefficient and rolling resistance torque in an attempt to reproduce the inter-locking and rolling resistance effects inherent to irregular particles. In these trials, the density and stiffness (Young's modulus) of the particles are set to values the same as those of quartz sand so that the particles are referred to as heavy and hard. Since the PMMA and TPU particles are typical light and soft particles, we carry out two additional trials using hard light and soft light particles, respectively, in order to assess the effects of the density and elastic modulus. The particles and walls are kept smooth in the last two trials. The naming convention of each trial is as follows: the first letter indicates the morphology of the particle (R represents rough, S represents smooth); the second letter indicates the roughness of the top and bottom walls (R represents rough, S represents smooth); the third letter indicates the hardness of the particle (H represents hard, S represents soft); and the fourth letter indicates the density of the particle (H represents heavy, L represents light). The parameters differentiating the numerical trials are listed in Table 2.

Instead of using expanding pressurized gas to disperse the particles,[23,24] the simulated particle rings are driven locally by a continuous input of energy restricted to the innermost layer of particles. This direct loading method has been used to simulate the propagation of a cylindrically symmetric blast wave in a dense granular gas as well as the shock initiation of instabilities in a one-dimensional granular slug.[14,40] Actually Kandan *et al.* found no fundamental differences between the coupled fluid/solid loading and direct loading in terms of the instability initiation in a shock impinged granular surface.[14] In line with the loading method adopted in the previous studies,[41,42] we apply the reflected shock pressure upon the inner surface of the particle ring measured in experiments to the particles residing along the internal perimeter as shown in Fig. 3(b). The magnitude of the force exerted on each particle is equal to the cross-section area of this particle multiplied by the overpressure, Δp, here Δp = 5 bar. Also the applied force vector aligns with the radial direction. A specific loading algorithm[41,42] was invoked to track the innermost layer of particles even when the internal surface becomes considerably corrugated, like the jagged configuration shown in Fig. 3(b).

Table 2 Key parameters in different numerical trials. μ_p: inter-particle friction coefficient; μ_{p-w}: particle–wall friction coefficient; $\mu_{r,p-p}$: coefficient of rolling friction between particles; $\mu_{r,p-w}$: coefficient of rolling friction between the particle and walls; ρ: material density; Y: Young's modulus

Descriptor	μ_p	μ_{p-w}	$\mu_{r,p-p}$	$\mu_{r,p-w}$	Y (GPa)	ρ (g cm^{-3})
RRHH	0.7	0.3	0.3	0.3	71.7	2.56
RSHH	0.7	0.1	0.3	0.01	71.7	2.56
SRHH	0.1	0.3	0.01	0.3	71.7	2.56
SSHH	0.1	0.1	0.01	0.01	71.7	2.56
SSHL	0.1	0.1	0.01	0.01	71.7	1.11
SSSL	0.1	0.1	0.01	0.01	7.17	1.11

D Verification of the numerical results

Due to the finite number of particles which can be reasonably modeled in the DEM simulation, the simulated particle rings are much thinner than those used in the experiments. During the experimental timescale (O(10^1) ms) the outgoing compaction front hasn't reached the external boundary of the particle ring yet, approximating an infinitely large medium condition. By contrast it only takes less than one millisecond for the compaction wave to travel through the simulated particle rings. The mismatch of timescales makes the direct comparison between the numerical results and experimental observations in terms of the evolution of the instability pattern quite challenging. The grain-scale simulations thus aren't aimed to reproduce the experimentally observed events. Instead we resort to simulations to uncover the grain-scale processes during the initiation of instabilities which occurs at very early instants. The early-time emergent instabilities have an explicit bearing on the resulting instability pattern at later times as will be discussed in Section III B.

To verify our simulations, we carried out complementary experiments and simulations using particle rings made up of the same materials and of the same geometry. Fig. 4(a) compares the trajectories of the internal and external boundaries of particle rings consisting of glass spheres attained by both experimental and numerical means. The dynamics of particle rings depicted by simulations is in line with that derived from the experiments despite the fact that the simulated particle ring expands a bit faster that the experimental one due to the continuous energy input as opposed to the quickly decaying pressure exerted on the particle rings in experiments. As to the particle rings consisting of rough irregular grains such as sand grains, we compare the typical growth rate of finger-like instabilities derived from both the experiments and simulations. As evident in Fig. 4(b), the simulated ''fingers'' grow at a similar rate to the experimentally observed ones, although the former grow a bit more slowly probably due to the lack of air

 This journal is © The Royal Society of Chemistry 2020

Published on 18 December 2019. Downloaded on 2/14/2020 10:45:36 AM.

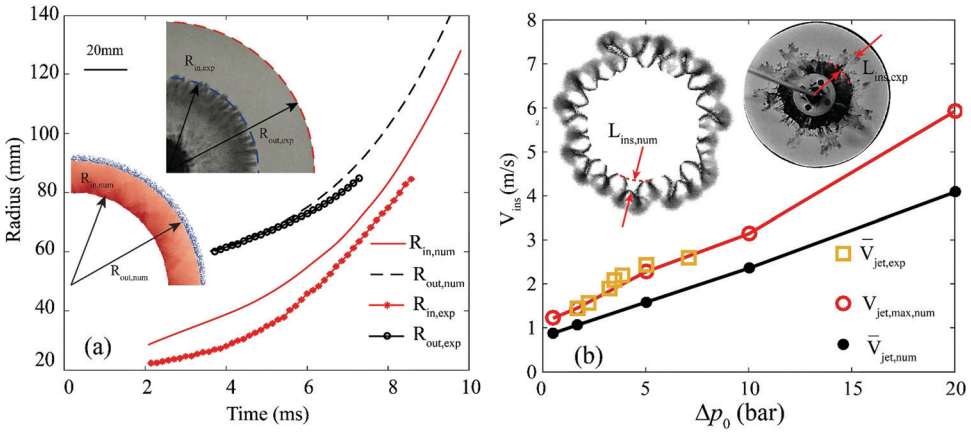

Fig. 4 (a) Trajectories of the internal and external surfaces of particle rings with D_{in} = 40 mm and D_{out} = 200 mm obtained from both experiments and simulations. $R_{in,num}$ and $R_{out,num}$ are the inner and outer radii of the simulated particle ring consisting of smooth particles confined by smooth walls; $R_{in,exp}$ and $R_{out,exp}$ are the inner and outer radii of the experimental particle ring consisting of glass spheres. (b) Growth rates of jet-like instabilities obtained from both experiments and simulations. $V_{jet,num,max}$ and $\bar{V}_{jet,num}$ are the maximum and average growth rates of instabilities in simulated particle rings consisting of rough particles confined by rough walls; $\bar{V}_{jet,exp}$ is the average growth rate of instabilities in experimental particle rings consisting of Sand #2 grains. The left and right insets in (b) present the configurations of shock dispersed particle rings in simulation and experiments, respectively.

erosion effects in the simulations. More verifications of the DEM simulations of shock loaded granular media can be found in ref. 41 and 42.

III. Results

A Formation of the instability pattern: experimental investigations

As the incident shock front transmits into the particles, the shocked particles are pushed and compacted into an annular compact band whose thickness depends on a variety of factors, including the flowability, initial packing fraction, compressibility, gap thickness and shock overpressure as well. With a sufficiently high spatial resolution, this compacted zone can be found using image analysis similar to the method used in ref. 25. The fronts of the compacted regions are indicated by the dashed circles in high-speed images of shock dispersed particles (see Fig. 5). It is worth noting that the outer boundary of the compacted annular band remains circular throughout regardless of the significant perturbation of the inner surface, which corroborates the azimuthal uniformity of the incident cylindrical shock front.

To better visualize the patterns formed by the disturbed internal surfaces of the particle rings, the original greyscale images are converted to binary images based on a luminance threshold. Fig. 5(a)–(f) present typical high-speed snapshots (top panels) of the particle rings subjected to the explosion and the corresponding binarized images (bottom panels). A well-defined pattern can be readily identified from the binarized images. Strikingly the pattern changes dramatically with the shocked granular media. The internal surface of the glass bead ring remains largely circular and stable, only short-wave undulation with small magnitude being detected. The pattern becomes noticeably corrugated for the PMMA bead ring, but still the "petals" of the pattern, namely the gas protrusions towards the external boundary, remain smooth and rounded. As the particle shape becomes increasingly irregular, the corresponding instability pattern becomes progressively complex and unstable, featuring a crumpled envelope, sharp cusps and frequent side-branching or tip-splitting. Specifically the Sand #1 pattern consists of a large number of stubby fingers studded with tiny offshoots which sprout alongside the elongation of major fingers. The fingers in the Sand #2 pattern appear much more slender, and constantly tip-split to generate new fingers as shown in Fig. 5(g). The unstable nature of the patterns exhibited by Sand #1 and #2 distinguishes them from the stable patterns formed in the glass bead, PMMA sphere and TPU particle rings, which is the focus in this paper. Another observation worth noting is that the magnitude of instabilities gets noticeably larger when the height of the glass bead rings is decreased from 4 mm to 2 mm (see Fig. 5(a) and (b)), with only 20 layers of grains across the height, implying increasingly stronger boundary effects for particle rings with shortened height. As will be discussed later the boundary effect would dominate the nature of the instability pattern in the simulated shock loaded short particle rings.

To quantify the evolution of the instability patterns, we define four characteristic length scales as shown in the sketch of Fig. 6(a): the outer radius of the annular compaction band, R_{comp}; the inner and outer radius of the distorted internal surface, R_{in} and R_{out}; and the magnitude of instabilities, $L_{ins} \equiv R_{out} - R_{in}$. The profile of the distorted internal surface derived from the binarized image is plotted in terms of $R(\theta)$ as presented in Fig. 6(b). R_{out} and R_{in} are calculated as the averages of the peaks and troughs identified from the R *vs.* θ curve (see Fig. 6(b)). Fig. 6(c) compares the normalized $R(\theta)$ scaled by the maximum values of $R(\theta)$ derived from well-developed destabilized internal surfaces of rings made up of glass beads (h = 4 and 2 mm), PMMA spheres and TPU particles. The increasingly enhanced fluctuations of $R(\theta)/R_{max}$ with increasing

Published on 18 December 2019. Downloaded on 2/14/2020 10:45:36 AM.

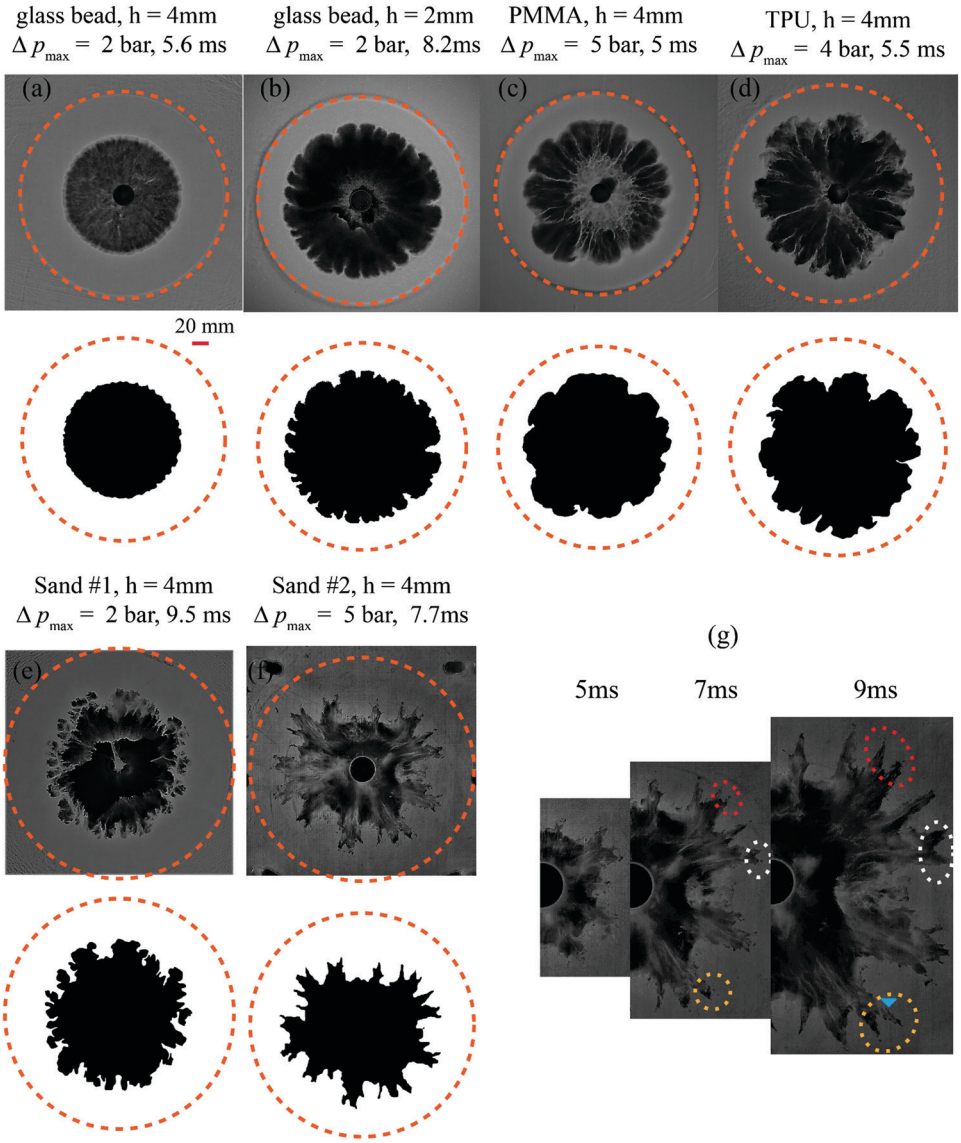

Fig. 5 Snapshots (upper panels) and the corresponding binarized images (lower panels) of the shock dispersed glass beads with h = 4 mm (a), glass beads with h = 2 mm (b), PMMA spheres with h = 4 mm (c), TPU particles with h = 4 mm (d), Sand #1 with h = 4 mm (e) and Sand #2 with h = 4 mm (f). (g) Evolution of the fingering instability pattern in Sand #2. The compaction fronts are denoted by the dashed circles (a–f). The tips of the instability fingers in (g) undergo tip-splitting.

irregularity of the particle shape and decreasing ring height quantitatively manifest the variation trend of instability patterns observed from Fig. 5. The characteristic length scales are inadequate to describe the unstable instability patterns in the Sand #1 and #2 rings, since besides the extension of the cusps, frequent side-branching or tip-splitting is also prevalent in the growth of the unstable ramified patterns.

Fig. 7(a) presents the trajectories of R_{in}, R_{out} and R_{comp} in the TPU particle rings subjected to divergent shock waves with $\Delta p_{exit,max}$ = 2 and 5 bar. After the initial acceleration phase with a duration of 2–3 ms, all characteristic length scales grow linearly with time. This linear growth mode also dominates the bulk of pattern growth regimes in other materials as demonstrated in Fig. 7(b). The instability patterns in PMMA and TPU particle rings grow faster than those in glass bead and sand rings (see Fig. 7(b)), suggesting that the material density could be a governing factor of the pattern growth rate. What is the most striking is that the ratio of R_{in} and R_{out}, R_{in}/R_{out}, converges to a plateau as R_{comp} increases for all samples as shown in Fig. 7(c) and (d). The magnitude of instabilities normalized with respect to R_{out}, $L_{ins}/R_{out} = 1 - R_{in}/R_{out}$, decreases with the peak overpressure (see Fig. 7(c)) and irregularity of the particle shape in the order of TPU powder (h = 4 mm), PMMA spheres (h = 4 mm), glass beads (h = 2 mm), and glass beads (h = 4 mm) (see Fig. 7(d)).

The consistency of R_{in}/R_{out} with increasing R_{comp} throughout the steady-state growth regime of the particle rings (see Fig. 7(c) and (d)) indicates that the distinguishable features of the instability pattern, namely R_{in}, R_{out} and R_{comp}, grow in direct proportion to each other. If there is no new generation of

 This journal is © The Royal Society of Chemistry 2020

Published on 18 December 2019. Downloaded on 2/14/2020 10:45:36 AM.

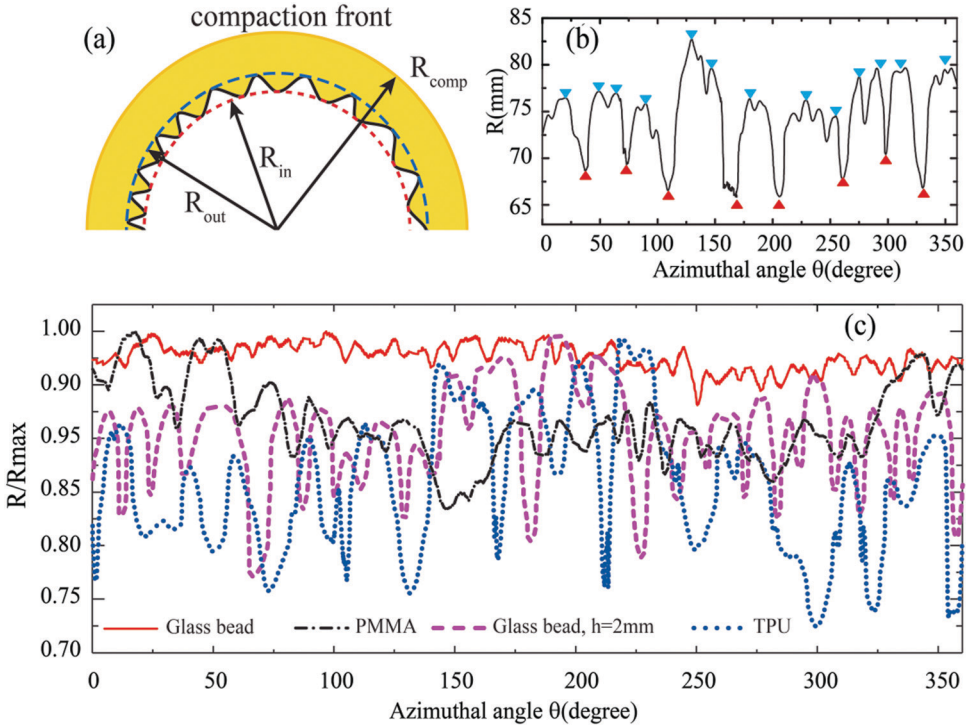

Fig. 6 (a) Illustration of the characteristic length scales defining the global instability pattern. (b) The radius *vs.* azimuthal angle curve, $R(\theta)$, along a typical distorted internal surface of TPU particles, the peaks (blue downward triangles) and troughs (red upward triangles) of the curve are averaged to be estimates of R_{in} and R_{out}, respectively. (c) Rescaled $R(\theta)$ by the maximum values for well-developed destabilized internal surfaces of rings of glass beads (h = 4 mm, red line), PMMA spheres (h = 4 mm, black dash dotted line), glass beads (h = 2 mm, purple dashed line) and TPU particles (h = 4 mm, blue dotted line).

instabilities emerging, which is the case for rings of glass beads, PMMA spheres and TPU powders, the overall pattern shape thereafter is kept unchanged, which is known as proportionate growth.[43,44] To demonstrate that the patterns indeed grow in a self-similar manner, Fig. 8(a) shows snapshots of the TPU pattern subjected to a shock with $\Delta p_{exit,max}$ = 2 bar at different times (the top row) and the left lower quarters of those same patterns which are magnified so that they all have the same compaction radii in the images (the second row). The enlarged images look essentially indistinguishable. In Fig. 8(b)–(e) we superimpose the profiles of the disturbed internal surfaces of rings made up of glass beads (h = 4 and 2 mm), PMMA spheres and TPU powders at different times (the third row). The scaled $R(\theta)/R_{max}$ *vs.* θ curves of the corresponding internal surfaces at different times are presented in the fourth row of Fig. 8. The scaled profiles of the internal surfaces at t = 4 ms and 5 ms for each sample agree well with each other. The fair resemblance of these profiles supported by the collapse of the azimuthal variations of the normalized profiles after the first 3–5 milliseconds corroborates the proportionate growth of the pattern recognized from Fig. 7(c) and (d).

Another point worth noting is that the TPU instability pattern seems on the verge of the stable-to-unstable transition since the cusps of the internal surfaces appear so crumpled that new instabilities may well be generated therein. The normalized magnitude of instabilities in TPU powder, L_{ins}/R_{out}, is around 0.16 with $\Delta p_{exit,max}$ = 2 bar (see Fig. 7(d)), which can be regarded as the first order estimate of the onset instability magnitude of the unstable instability pattern. Indeed the normalized magnitude of instabilities in the unstable pattern for Sand #2 is well beyond this threshold, $(L_{ins}/R_{out})_{Sand\ \#2} \sim 0.46$.

On the macroscale granular media are often modeled as viscoplastic fluids without taking into account the inherent heterogeneities.[45] Thus the divergent shock loading induces incompressible homogeneous divergent flows inside the shock compacted granular medium. Based on this assumption we propose a continuum model to account for the proportionate growth mode dominating the stable instability pattern, in which the granular flows are described by the $\mu(I)$ rheology.[45] The formulation of the model and the parametric analysis are detailed in Appendix B. Here we only highlight the most significant implication. The stable proportionate growth only allows perturbations with insignificant magnitude. This analytical prediction suggests that the magnitude of initial disturbances developed during the prior transient phase is of significance to the ensuing stable self-similar growth mode, which is consistent with the findings of Kandan *et al.*[14] Be aware that the continuum model only accounts for the steady-state growth regime of surface instabilities with the assumption of homogeneous divergent flows dominating the shock compacted particles. This assumption is to be challenged by the DEM investigations below, which find that this assumption only holds for

Published on 18 December 2019. Downloaded on 2/14/2020 10:45:36 AM.

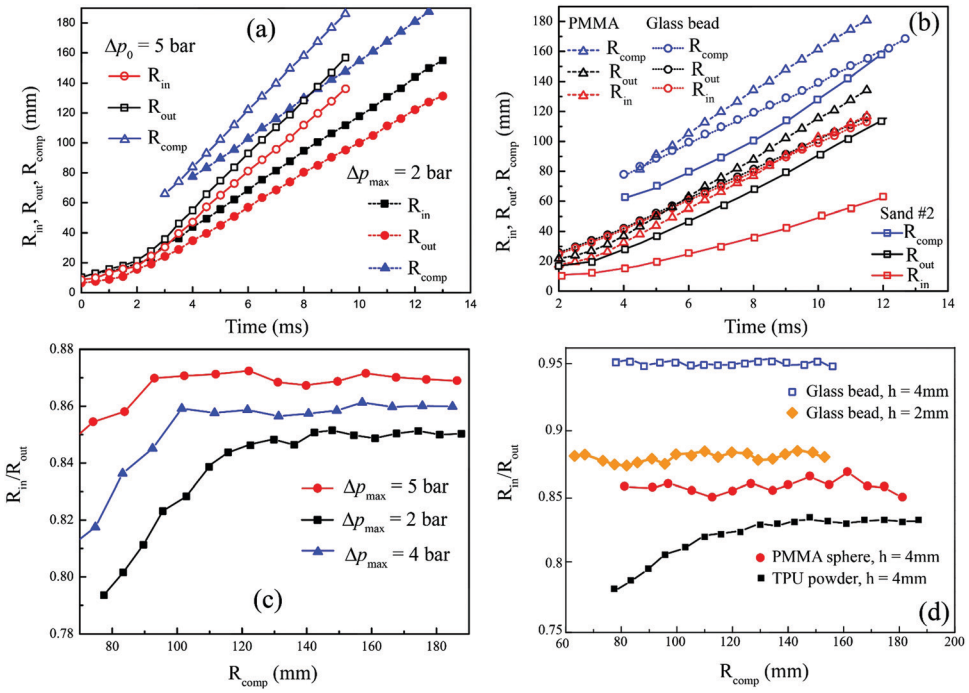

Fig. 7 (a) Temporal variations of R_{in}, R_{out} and R_{comp} in the TPU particle rings subjected to shocks with $\Delta p_{exit,max}$ = 2 and 5 bar. (b) Temporal variations of R_{in}, R_{out} and R_{comp} in glass bead, PMMA sphere and Sand #2 grain rings subjected to the shock of $\Delta p_{exit,max}$ = 2 bar. (c) Variations of R_{in}/R_{out} with R_{comp} in the TPU particle rings subjected to shocks with varying overpressure. (d) Variations of R_{in}/R_{out} with R_{comp} in glass bead (h = 4 mm), glass bead (h = 2 mm), PMMA sphere and TPU grain rings subjected to the shock of $\Delta p_{exit,max}$ = 2 bar.

the particles confined in the Hele-Shaw cell with good flowability.

B Stable-to-unstable transition of the instability pattern: grain-scale simulations

Due to the fact that the simulated particle rings are much thinner than those in experiments, the DEM simulations are only capable of studying the dynamics of particles at very early instants upon the shock loading, specifically the first millisecond when the compaction front is about to reach the external boundary of the ring. As stated by Kandan *et al.*,[14] the structure of the initial disturbances is crucial to the ensuing development of surface instabilities; the distinct late-time growth modes of instabilities observed in our experiments ought to be directly linked to the inception phase during which the incipient instabilities are generated upon the shock impinging the smooth surfaces of the particle rings.

Fig. 9 presents the evolution of the coarse-grained velocity fields in all six numerical trials during the first millisecond. These trials can be readily categorized into two groups in terms of flow patterns, which can be characterized as localized shear flows and homogeneous divergent flows, respectively. Particles confined between two rough walls (trials RRHH and SRHH) are substantially dominated by localized shear flows regardless of the roughness of the particles (see Fig. 9(a) and (c)). The localization of flows commences as early as the first dozens of microseconds while the internal surface of the ring remains smooth and circular. At later times, the internal surface progressively gets folded inwards where the localized flows are intensified, evolving into a jagged configuration. By contrast homogeneous divergent flows are largely sustained in particles confined by smooth walls (trials RSHH, SSHH, SSHL and SSSL, see Fig. 9(b), (d)–(f)). Note that the petal-like structure shown in the velocity fields in Fig. 9(b), (c)–(e) is the signature of shear bands, which are the well-known failure form observed in radial dilation and hydraulic fracture of continuum media.[46,47] Thereby at later times small undulations occur wherever the shear bands coalesce. The density and the Young's modulus seem to play a trivial role in terms of determining the nature of the velocity field.

To quantitatively correlate the localized flows and the ensuing surface instabilities, we superimpose the azimuthal variations of the well-defined velocity profile and the radius of the internal perimeter of the ring for trial RRHH at t = 3 ms in Fig. 10(a). The positions of the velocity peaks corresponding to the localized flows coincide with the cusps of the internal surface as evident in Fig. 10(a). Prior to the establishment of the persistent pattern of localized flows, neighboring localized flows likely coalesce into stronger ones while strong localized flows probably annihilate the adjacent small ones as indicated in Fig. 10(b).

The trajectories of the internal and external surfaces of the rings, R_{in} and R_{out}, in typical numerical trials are shown in Fig. 11(a). In trials RRHH and SRHH in which localized flows are prevalent R_{in} increasingly lags behind R_{out}. At later times R_{out} grows linearly with time while R_{in} increases at a much slower rate, most growth occurring at the cusps of the disturbed internal surface. As a result, the normalized length of instabilities, L_{jet}/R_{in}, grows exponentially with R_{in} as shown in Fig. 11(b).

 This journal is © The Royal Society of Chemistry 2020

Published on 18 December 2019. Downloaded on 2/14/2020 10:45:36 AM.

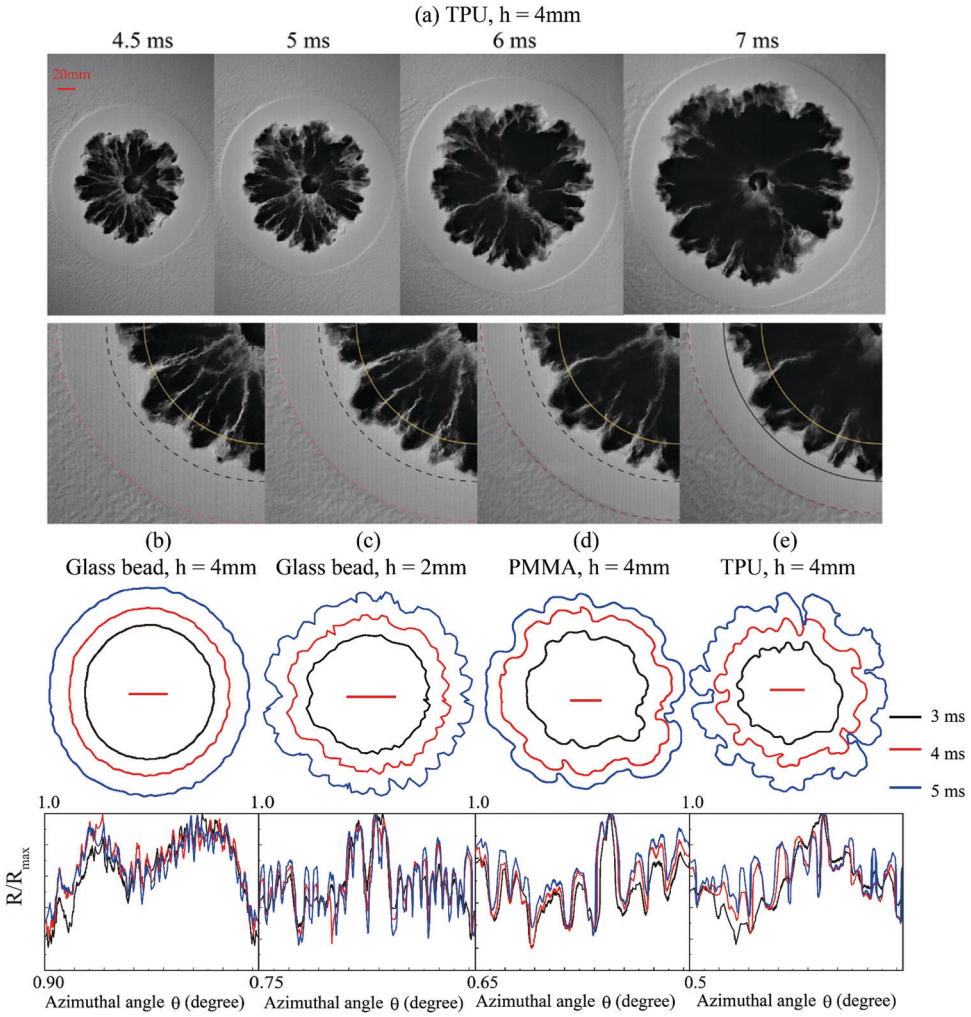

Fig. 8 (a) Snapshots (first row) and enlarged left lower quarter of the corresponding snapshots (second row) of the shock dispersed TPU powder ring with $\Delta p_{exit,max}$ = 2 bar at different times. (b–e) (third row) Superimpositions of profiles of interface surfaces of rings made up of glass beads h = 4 mm (b), glass beads h = 2 mm (c), PMMA spheres h = 4 mm (d) and TPU powder h = 4 mm (e) at different times. The collapse of the scaled $R(\theta)$ of the distorted internal surfaces corresponding to (b–e) at different times is presented in the fourth row. The scales in (b–e) represent 20 μM.

The runaway growth of incipient instabilities gives rise to the unstable growth mode of the instabilities observed in experiments. By contrast, thanks to the homogeneous divergent flows (trials RSHH and SSHH) the trajectories of R_{in} closely trail those of R_{out} with barely discernible gaps. The normalized length of instabilities, L_{jet}/R_{in}, hence remains on a quite low plateau and only picks up when the macroscale shear band failures become prevalent (see Fig. 11(b)). The insignificant magnitude of instabilities which barely changes with regard to the expanding internal surface is necessary for sustaining the ensuing stable growth regime of instabilities as suggested by both experimental observations and the analytical model.

The well-defined instability patterns arising from these two distinct flows can be readily distinguished from Fig. 11(c). The disturbed internal surfaces in trials RRHH and SRHH form jagged patterns with regularly spaced sharp cusps which arise from the localized shear flows induced by the rough boundaries. By contrast, slightly undulating patterns with irregular small oscillations are the result of the largely homogeneous divergent flows guaranteed by smooth boundaries. Note that the combination of rough particles and rough boundaries produces the sharpest instability pattern.

One follow-up question to be addressed is what are the grain-scale processes responsible for the fundamental changes of flow patterns induced by the roughness of boundaries? Inarguably the particle flows are closely correlated with the complex force network in granular systems. Fig. 12(a)–(d) present configurations of typical force chains in trials RRHH, RSHH, SRHH, and SSHH, respectively. Since the simulated particle rings only have about two layers of particles across the height, the particles in contact with the top and bottom boundaries denoted by filled circles in Fig. 12(a)–(d) constitute the bulk of force chains, whereby the particle–wall friction plays an integral part in the force structure. Rough boundaries are very likely to arrest particles in contact so that the particle rearrangement is impeded and the force chains are terminated at particles stuck on boundaries. This scenario is illustrated in Fig. 12(e) in which force chains prematurely end with particles

Published on 18 December 2019. Downloaded on 2/14/2020 10:45:36 AM.

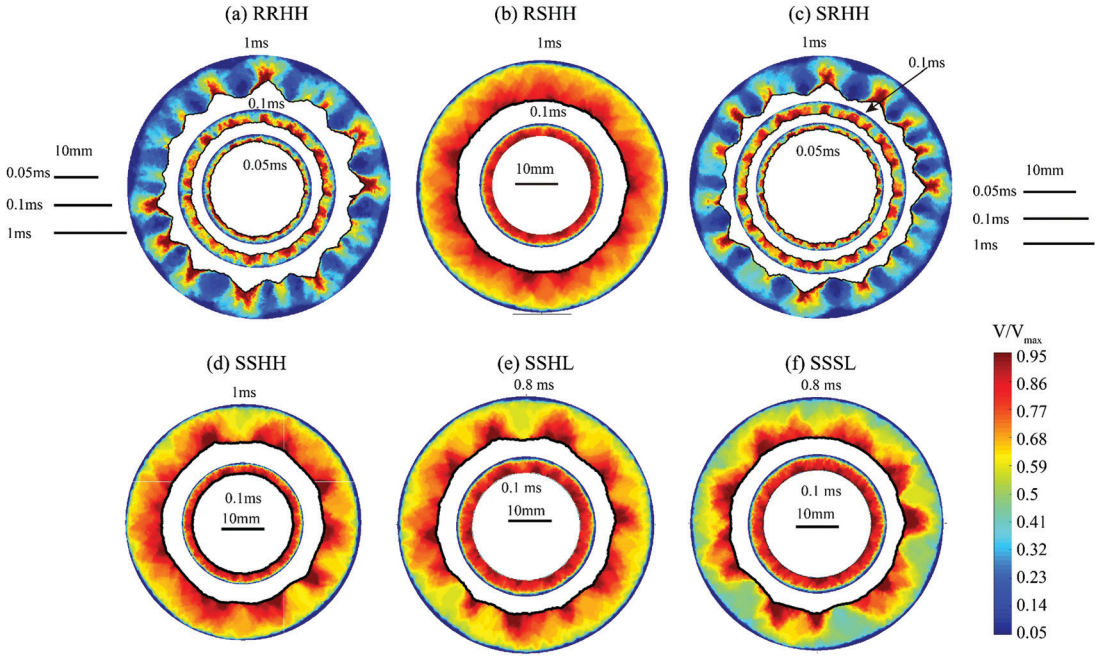

Fig. 9 Normalized coarse-grained velocity fields in all six numerical trials during the first millisecond. Velocities are normalized by the corresponding maximum values.

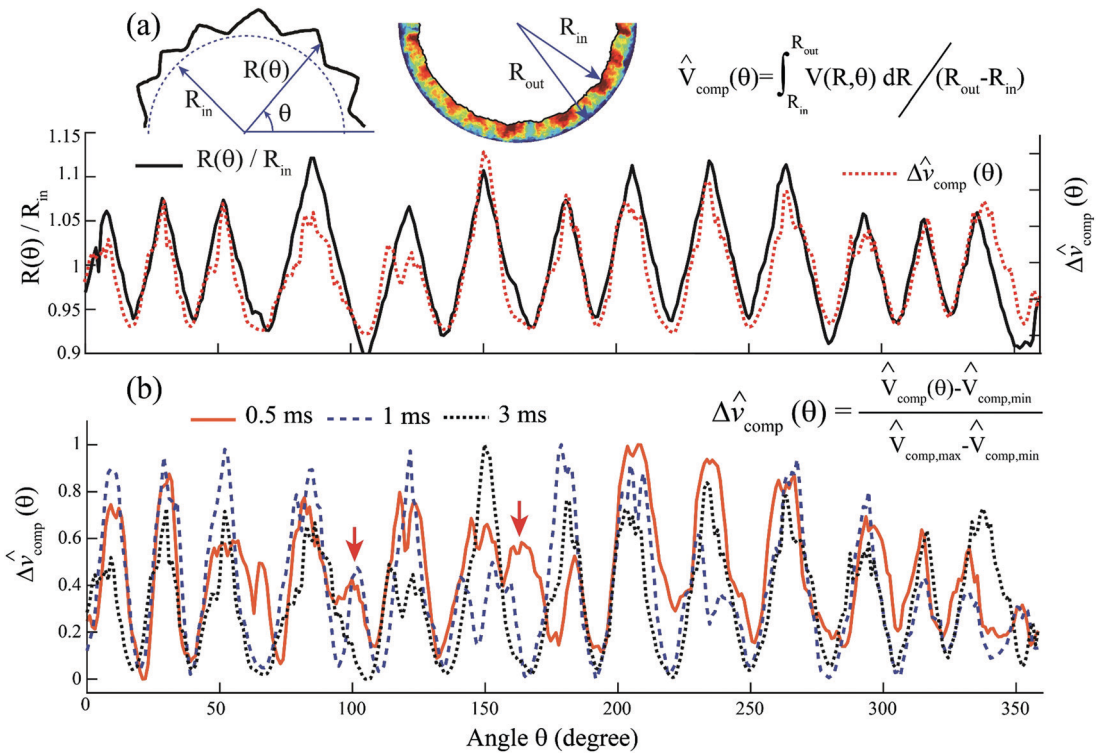

Fig. 10 (a) Comparison of azimuthal variations in the normalized radially averaged velocity fluctuations inside the compaction band, $\Delta\hat{v}_{\mathrm{comp}}(\theta) = \frac{\hat{v}_{\mathrm{comp}}(\theta) - \hat{v}_{\mathrm{comp,min}}}{\hat{v}_{\mathrm{comp,max}} - v_{\mathrm{comp,min}}}$, and the normalized radii of points constituting the disturbed internal surface in trial RRHH, $R(\theta)/R_{\mathrm{in}}$, at t = 3 ms. (b) Evolution of $\Delta\hat{v}_{\mathrm{comp}}(\theta)$ at different times in trial RRHH. The velocity peaks indicated by the arrows in (b) are annihilated at later times.

A and B stuck on the top and bottom boundaries. By contrast, in trials with smooth boundaries particle rearrangement takes place with little hindrance. Force chains quickly extend through the space between the top and bottom boundaries as schematized in

 This journal is © The Royal Society of Chemistry 2020

Published on 18 December 2019. Downloaded on 2/14/2020 10:45:36 AM.

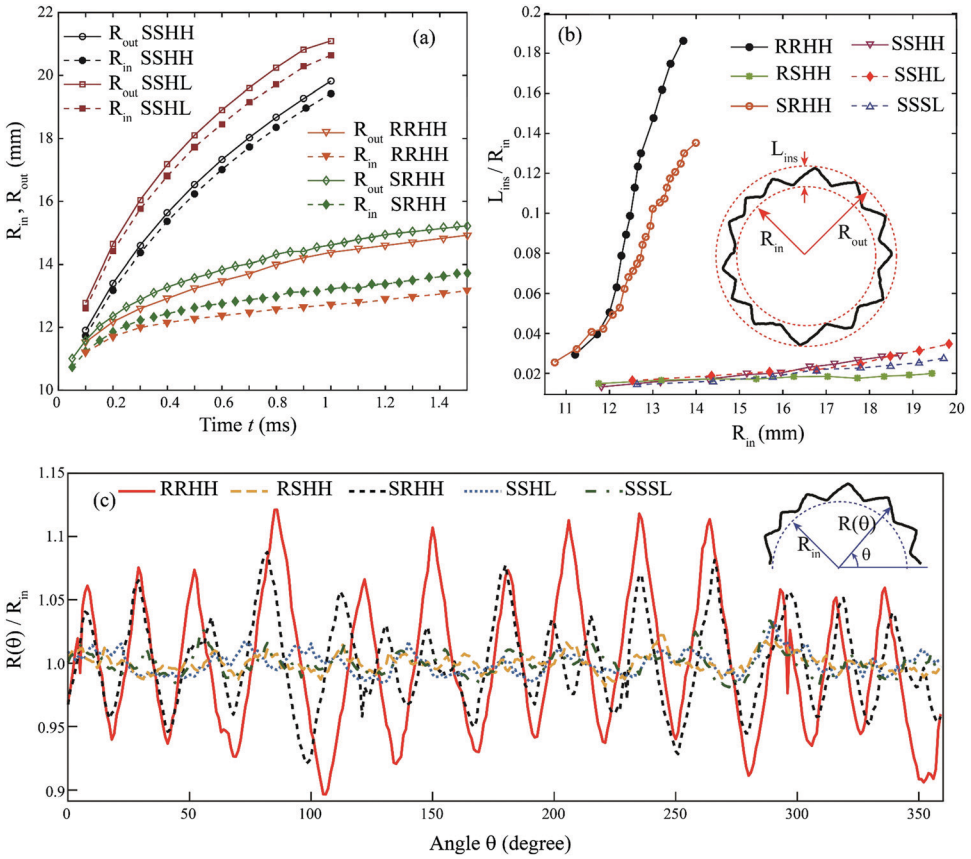

Fig. 11 (a) Temporal evolutions of R_{in} and R_{out}, (b) variations of the normalized magnitude of instabilities, L_{jet}/R_{in}, with R_{in}, and (c) azimuthal variations of the normalized radii of points constituting the internal surfaces of the rings, $R(\theta)/R_{in}$, in numerical trials.

Fig. 12(f), encompassing most of the particles in their paths. The significant boundary effects on the force chains are evident in Fig. 12(a)–(d). The typical force chains in trials RRHH and SRHH are short and sparse (see Fig. 12(a) and (c)) in contrast with the long extended branched force chains in trials RSHH and SSHH (see Fig. 12(b) and (d)).

The sparse short force chains in trials with rough boundaries (trials RRHH and SRHH) constitute sparse chain-like force networks with diffusive boundaries as presented in Fig. 13(a) and (b). The depiction method of the force network is detailed in the caption of Fig. 13. The sparsely dispersed strong force chains transmit more momentum into the grains connected by chains. These particles hence move faster than their neighbors, forming incipient localized flows as shown in Fig. 13(a). The localized flows flare out at the tip, inducing transverse flows. Adjacent counter transverse flows give rise to granular vortices therein as indicated in Fig. 13(b). The intensified granular vortices substantially dissipate the energy therein so that particles participating in vortices barely move. As indicated by the coarse-grained kinetic energy profiles corresponding to the respective velocity profiles (see Fig. 13(e)), minimal energy is deposited in the granular vortices. A pattern consisting of well separated localized shear flows emerges. The formation and evolution of granular vortices are elucidated in ref. 41 and 42. By contrast, a much denser force network with a well-defined boundary dominates the dynamics of particles confined between smooth boundaries as shown in Fig. 13(c) and (d). Almost the entire collection of particles is percolated by the dense force network and flows divergently like granular fluids as illustrated by Fig. 13(c) and (d). Thereby homogeneous divergent flows are sustained. The kinetic energy is evenly distributed throughout the shock compacted particle band (see Fig. 13(f)).

Since the spatial heterogeneities of non-linear force chains sustained and enhanced by the rough walls nucleate incipient instabilities, namely localized shear flows, evaluating the characteristic length of these spatial heterogeneities would greatly deepen the understanding of the wavelength selection mechanism of the instability pattern. Indeed the spatial structures of force networks in particles confined by the rough and smooth walls (trials RRHH and RSHH) exhibit substantially different spatial features and undergo distinct evolutions as shown in Fig. 14(a) and (b). In the present work, the characteristic spacing between largely radially aligned force chains properly defines the length associated with the spatial heterogeneities of the force structure. To this end the spatial Fourier power spectra of the coarse-grained contact force field are analyzed. The average wavelength $\hat{l}_p$ of the force structure is calculated following a procedure explained hereafter. First the discrete Fourier transform and the power spectrum of the coarse-grained magnitude of the contact force $S(k,R_i)$ at each concentric annular band R_i with a

Published on 18 December 2019. Downloaded on 2/14/2020 10:45:36 AM.

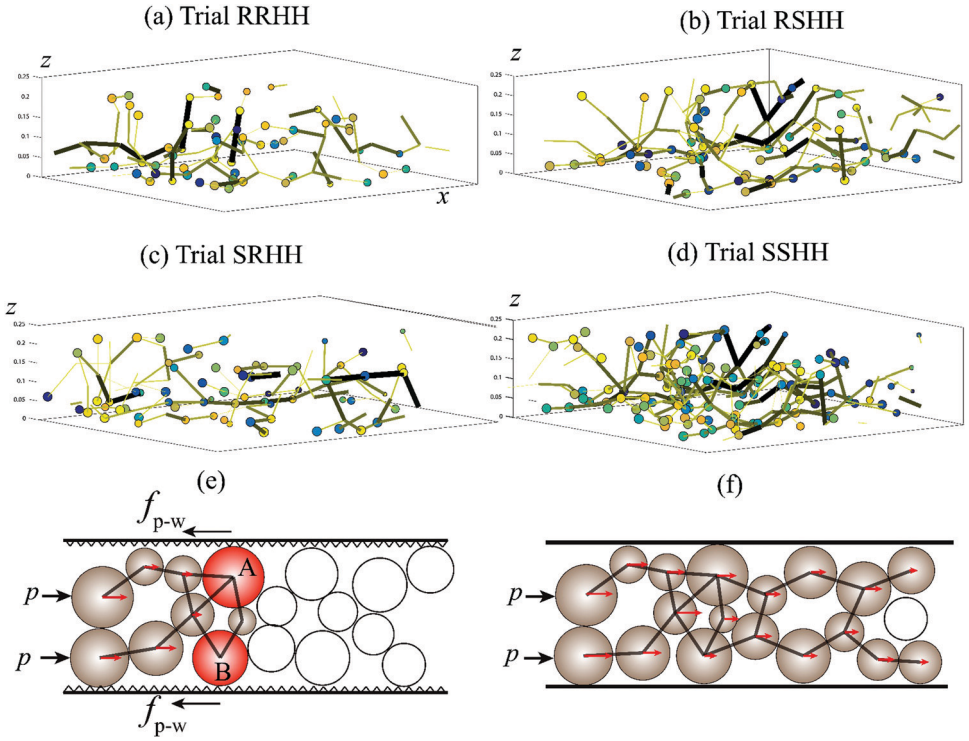

Fig. 12 Snapshots of segments of force networks in trials RRHH (a), RSHH (b), SRHH (c), and SSHH (d). The lines denoting force chains have varying thickness and shade in accordance with the force magnitude. Particles in force networks which are in contact with boundaries are denoted by filled circles. How the rough boundaries give rise to short force chains is schematized in (e). (f) illustrates the long extended force chains alongside the rapid particle rearrangement with the presence of smooth boundaries.

thickness of one particle diameter inside the compaction front are evaluated, where k is the wave number. The average power spectrum, $S(k)$, is then obtained by averaging over all power spectra. The average wave number is defined as $\langle k \rangle = \sum (k\bar{S}(k))/\sum \bar{S}(k)$. The average wavelength $\hat{l}_p$ is the reciprocal of the average wave number. Fig. 14(c) presents the radial variations of normalized wavelength l_p/d_p in trials RRHH and RSHH at t = 0.05 and 0.1 ms. In contrast with the consistent low values of $l_p(R)$ throughout the compact band in trial RSHH, $l_p(R)$ quickly rises up towards the compaction front in trial RRHH, indicating some singularly long force chains extending into the bulk. The temporal evolutions of $\hat{l}_p$ in these two trials are plotted in Fig. 14(d). The initial wavelength of the force chains is insensitive to the roughness of the walls, $\hat{l}_p \sim 7.5d_p$. $\hat{l}_p$ in trial RSHH converges to a constant value $\hat{l}_p \sim 6.5d_p$ after an initial transient compaction phase. By contrast, $\hat{l}_p$ in trial RRHH continues to increase, indicating a persistent coarsening evolution as illustrated in Fig. 14(a). Actually the localized flows arising from the heterogeneous stress transmission and the resulting mesoscale packing variations propel the continuous coarsening of the force structure.

The particle-scale heterogeneous force networks aforementioned are also manifested in the mesoscale coarse-grained pressure profiles as shown in Fig. 15. Consistent with the distinctive characteristics of force networks shown in Fig. 13 and 14 the pressure profiles in trials with rough boundaries (Fig. 15(a)) feature sporadic stout high pressure protrusions emanating from the internal surface in contrast with the dense prolonged high pressure "fingers" in trials with smooth boundaries (Fig. 15(b)). These branched fingers are connected to each other, forming an extended high pressure annular zone. Thereby the azimuthally averaged pressure rapidly drops across the width of a narrow compaction band in trials with rough boundaries, whereas the pressure decreases much more slowly inside a much extended compact band in trials with smooth boundaries (see the insets in Fig. 15(a) and (b)).

As discussed above, the strong wall–particle friction impedes prompt particle rearrangement, leading to a sparse chain-like force network. Thereafter the grain-scale heterogeneities in terms of momentum transmission would not be eliminated fast enough, enabling the activation of localized shear flows, which leads to substantial macroscopic instabilities. The promptness of particle rearrangement, or in general the flowability of particles through a narrow space, ought to be the most crucial dominant factor underlying the stable-to-unstable transition of the instability pattern.

The DEM simulations in this work only involve about two layers of particles across the height. Hence it is the wall–particle friction rather than the inter-particle friction that plays an overwhelming role in the flowability of such short particle rings. But in real world systems, the geometric length of the confinement should be several orders larger than the particle size. The inter-particle interaction more likely determines the flowability of particles. Specifically the angularity of particles would give rise to substantial inter-particle locking that restrains

 This journal is © The Royal Society of Chemistry 2020

Published on 18 December 2019. Downloaded on 2/14/2020 10:45:36 AM.

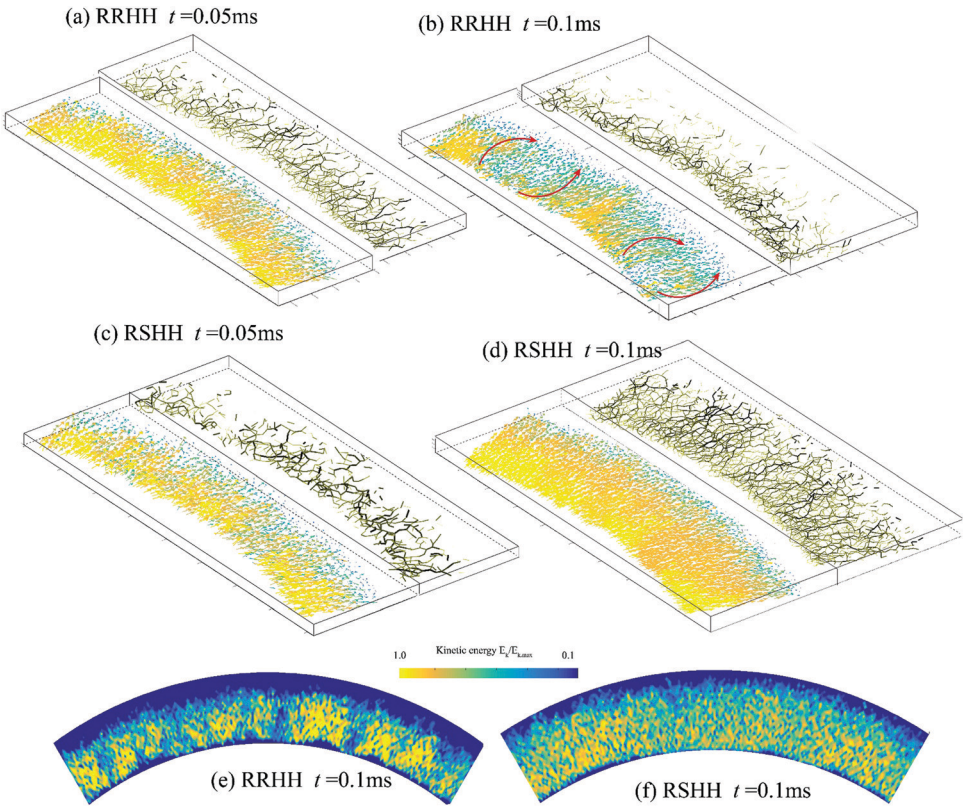

Fig. 13 Snapshots of segments of particle velocity fields (left panel) and force networks (right panel) in trials RRHH (a and b) and RSHH (c and d) at different times. (e) and (f) are profiles of the coarse-grained kinetic energies scaled by the maximum values corresponding to (b) and (d), respectively. The depiction method of force chains in this paper is as follows: the thickness and shade of lines representing the force chains linearly scale with the logarithm values of the contact forces. Weak contacts with the magnitude of the contact force in the bottom 20% bracket are ignored.

relative sliding and rotation between particles, and thereby the flowability of the particles is significantly reduced. In line with the above deduction, the spherical glass beads and PMMA spheres with the lowest flow energy and wall–particle friction are able to sustain stable instability patterns with small disturbances. By contrast the two types of quartz sand have substantially higher flow energy and wall–particle friction as well, thus most likely developing unstable instability patterns. The angular TPU powder has high flow energy but moderate wall–particle friction, whose instability pattern probably exhibits mixed characteristics. Indeed the experimental observations support these predictions.

IV Discussion

The flowability of particles involves the competition between two timescales related to the microscopic rearrangements and macroscopic deformation, respectively. The macroscopic deformation in this context can be measured by the expansion of the compaction band driven by the incident shock wave. The promptness of particle rearrangement dictates how quickly the particles in the wake of the compaction front adapt to the bulk expansion. The particle systems in which particle rearrangement is fast compared with the macroscopic deformation act analogously to fluids; homogeneous divergent flows are maintained inside the compaction band. Otherwise, inhomogeneous flows originating from the heterogeneities of momentum transmission are sustained by the slow particle rearrangement. In this case, the grain-scale heterogeneities of granular media overwhelm the continuum approximation of granular flows.

The microscopic time scale of particle rearrangement is often described by the time it takes for a particle to fall in a hole of particle size d_p under pressure P[45]

$$t_{mi} = \frac{d_p}{\sqrt{P/\rho_p}}. \quad (3)$$

This derivation is appropriate for monodisperse dry spheres, while it fails to account for the effects of irregular shape and confinement. The inter-particle locking owing to the angularity of particles and the hindrance by rough boundaries of the particle motion entail a longer duration for the particle rearrangement,[34] which ought to be probably considered in our studies. The macroscopic deformation, represented by the radial expansion of the compaction band, depends on both the pressure gradient developed in the granular systems by the incident shock waves and the mass of compacted particles. The former is closely related to the overpressure of the incident shock and the permeability of the shock compacted particles.[48]

Published on 18 December 2019. Downloaded on 2/14/2020 10:45:36 AM.

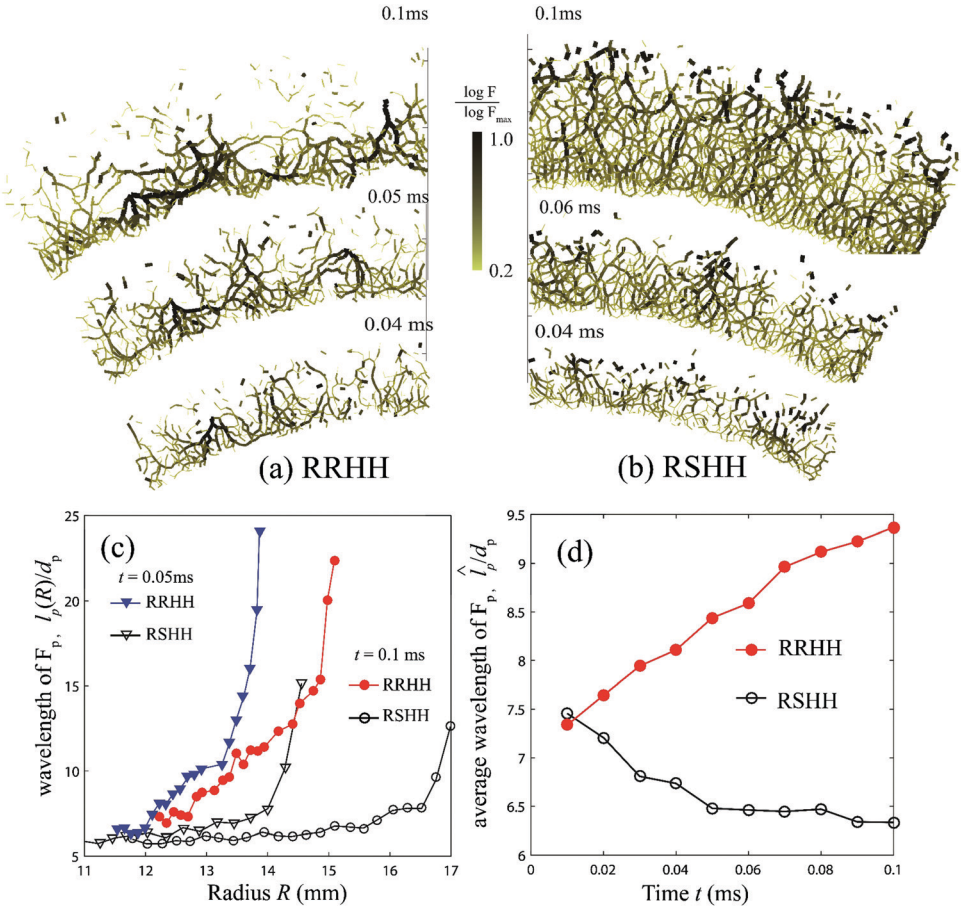

Fig. 14 Snapshots of segments of force networks in trials RRHH (a) and RSHH (b) at different times. (c) Radial variations in the (azimuthal) wavelengths of force chains in trials RRHH and RSHH at t = 0.05 and 0.1 ms. (d) Temporal evolutions of the average (azimuthal) wavelengths of force chains in trials RRHH and RSHH.

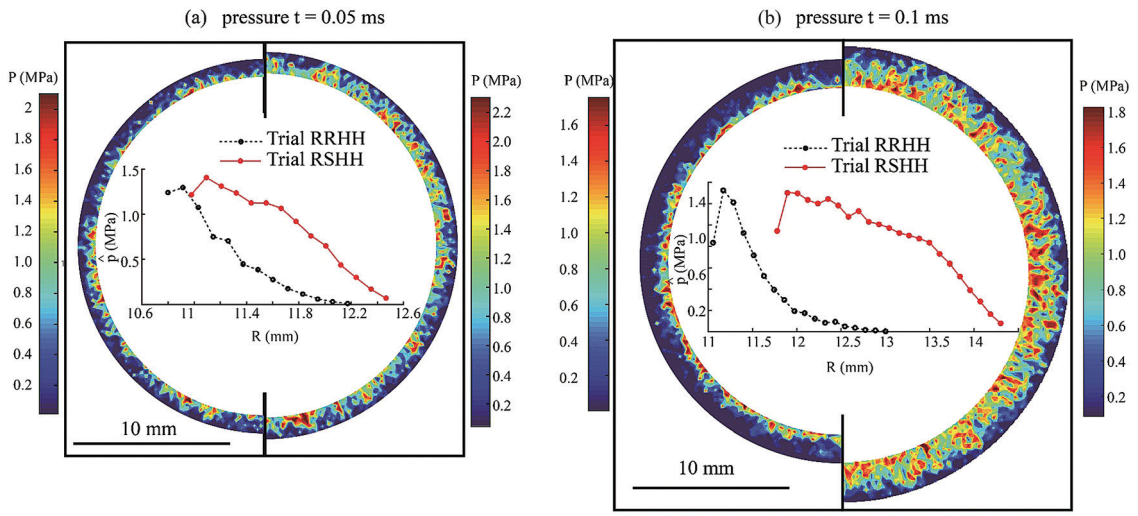

Fig. 15 Coarse-grained pressure fields in trial RRHH (left panel in each sub-figure) and RSHH (right panel in each sub-figure) at t = 0.05 ms (a) and 0.1 ms (b). Insets: Radial variations in the azimuthally averaged pressure in trials RRHH and RSHH.

The latter depends on the compressibility of the particles and the transmissibility of forces from particle to particle,[35] both varying from packing to packing. Specifically, angular and rough particles tend to form long and entangled force chains so that a higher volume is required to be mobilized as the internal surface of the particle layer moves. The shock

 This journal is © The Royal Society of Chemistry 2020

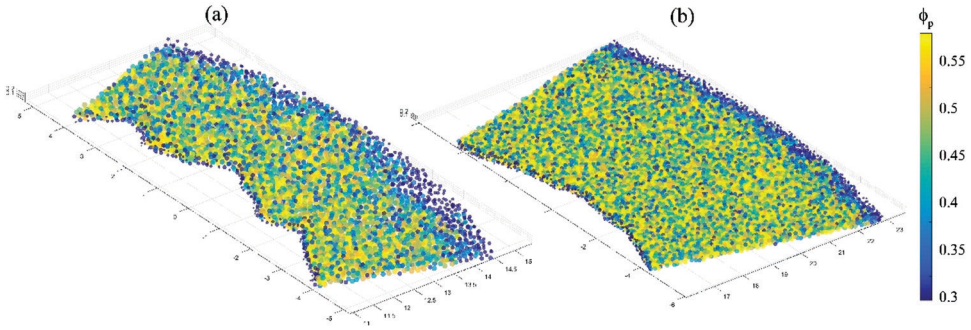

Fig. 16 Snapshot of segments of shock compacted particles in trials RRHH (a) and SSHH (b) where the particles are colored by the local packing fraction.

Published on 18 December 2019. Downloaded on 2/14/2020 10:45:36 AM.

compaction for various granular systems should be the subject of further work.

The current DEM simulations did not incorporate gas infiltration and load transfer between gas in voids and particles, such that the compressive stresses in the granular phase may well be noticeably reduced.[48] But we argue that the gaseous pressure dependent on the local permeability serves as the background pressure which solely doesn't bring about heterogeneous particle dynamics in an initially homogeneous packing. Fig. 16 shows the shock compacted particles in trials RRHH and SSHH where the particles are colored according to the packing fraction. We use Voronoi tessellation (obtained with Voro++[49]) to calculate the local, instantaneous packing fraction of each particle, ϕ_p, defined as the particle's volume divided by its Voronoi cell. ϕ_p varies on the grain-scale in both trials. There are no detectable meso-scale differences of ϕ_p induced by the localized flows (trial RRHH) compared with the ϕ_p profile in homogeneous divergent flows (trial SSHH). Hence the gaseous pressure associated with the gas diffusion remains homogeneous on the meso-scale even in the localized flows, making a trivial contribution to the localized particle dynamics.

V Summary

In the present work, we investigate the morphodynamics of instability patterns emerging from a shock impinged granular interface from both macroscopic and microscopic perspectives. Special efforts are focused on the transition of a stable pattern governed by proportionate growth to an unstable fingering pattern with prevalent tip-splitting. The grain-scale simulations find that the stable-to-unstable transition of the instability pattern arises from the shift of the granular dynamics from homogeneous divergent flows to substantial localized flows, which in turn is associated with the distinctive spatial structure of the force network in particles confined in a Hele-Shaw cell. If the particle rearrangement is significantly impeded by the rough boundaries or angularity of grains, the emergent force chains are short and spatially sparse and inhomogeneous, rendering heterogeneities in terms of momentum transmission which eventually evolve into localized flows. If the particles are more prone to fluidize, the force networks become more extended and spatially dense and homogeneous, sustaining the homogeneous divergent flows. More generally, we argue that it is the macroscopic flowability of particles through narrow spaces which embodies the competition between the particle rearrangement and macroscopic deformation that is the primary factor determining the morphodynamics of the granular instability pattern.

Conflicts of interest

There are no conflicts to declare.

Appendix A: Formulation of the Hertz–Mindlin contact model

The Hertz–Mindlin contact model is a variant of the non-linear spring–dashpot contact model based on the Hertz–Mindlin contact theory. For two spherical particles in contact, i and j, the forces between them, F_p, consist of normal and tangential components, namely F_n and F_t, which are composed of non-linear elastic and viscous damping elements as calculated by the equations as follows

$$F_n = k_n\delta_n - \gamma_n\Delta V_n \tag{4}$$

$$F_t = \begin{cases} k_t\delta_t - \gamma_t\Delta V_t & \text{if} \quad F_t < \mu_s F_n \\ \dfrac{\mu_s|k_n\delta_n|\delta_t}{|\delta_t|} \end{cases} \tag{5}$$

F_t becomes constant once F_t calculated by the first expression of eqn (5) is beyond the Coulomb friction limit governed by the product of the sliding friction coefficient μ_s and F_n. In eqn (4) and (5), δ_n is the overlap distance of particle i and j, $\delta_n = R_i + R_j - l_{ij}$, where R_i and R_j are the radii of particles i and j, respectively, and l_{ij} is the distance between the centers of two particles. δ_t is the tangential displacement between two particles in contact for the contact duration. k_n and k_t are the stiffnesses for the normal and tangential contact, respectively. γ_n and γ_t are the viscoelastic damping constants for the normal and tangential contact, respectively. ΔV_n and ΔV_t are the normal and tangential components of the relative velocity of particles in contact, respectively.

Fig. 17 illustrates δ_n and δ_t at one instant during the contact process of two spheres. Compared with the explicit definition

Published on 18 December 2019. Downloaded on 2/14/2020 10:45:36 AM.

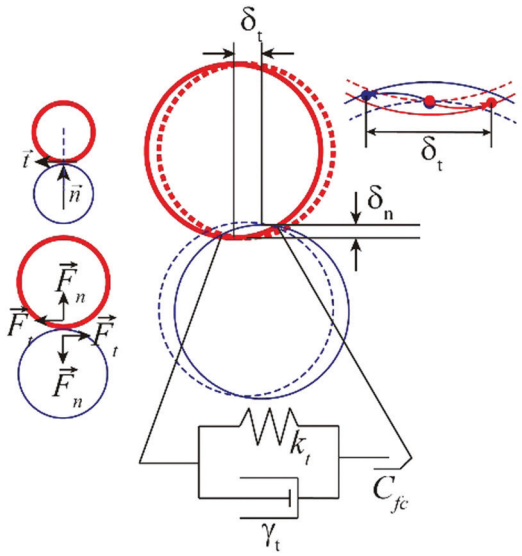

Fig. 17 Illustration of δ_n and δ_t in the Hertz–Mindlin contact model. The insets show the directions of $\vec{n}$, $\vec{t}$, $\vec{F}_n$, and $\vec{F}_t$.

of δ_n, the derivation of δ_t appears subtler. First we calculate the tangential component of the velocity of particle j relative to particle i at the contact point, $\Delta V_{t,C}$, by eqn (6) and (7)

$$\Delta V_{t,C} = \Delta \vec{V}_C \cdot \vec{t} \tag{6}$$

$$\vec{t} = \frac{\Delta \vec{V}_C - \left(\Delta \vec{V}_C \cdot \vec{n}\right)\vec{n}}{\left|\Delta \vec{V}_C - \left(\Delta \vec{V}_C \cdot \vec{n}\right)\vec{n}\right|} \tag{7}$$

where $\Delta \vec{V}_C$ is the velocity of particle j relative to particle i at the contact point, $\vec{n}$ is the unit vector normal to the tangent plane of two particles through the contact point, and $\vec{t}$ is the unit vector aligned with the direction of $\Delta \vec{V}_{t,C}$. δ_t is the integration of $\Delta V_{t,C}$ from the time when the two particles first came into contact, t_0, to the current time, t (see eqn (8)).

$$\delta_t = \int_{t=t_0}^{t} \Delta V_{t,C} \mathrm{d}t \tag{8}$$

$\vec{F}_n$ is the repulsive force perpendicular to the tangent plane at the contact point of two spheres. $\vec{F}_t$ is in the tangent plane and perpendicular to $\vec{t}$. Fig. 17 also illustrates the directions of $\vec{F}_n$ and $\vec{F}_t$. Note that the unit tangential direction, $\vec{t}$, may change during the contact as well as $\vec{t}$. The coefficients k_n, k_t, γ_n and γ_t are calculated using eqn (9)

$$\begin{cases} k_n = \frac{4}{3} Y_{ij}^* \sqrt{R_{ij}^* \delta_{n_{ij}}} \\ k_t = 8 G_{ij}^* \sqrt{R_{ij}^* \delta_{n_{ij}}} \\ \gamma_n = -2\sqrt{\frac{5}{6}} \beta \sqrt{S_{ij,n} m_{ij}^*} \\ \gamma_t = -2\sqrt{\frac{5}{6}} \beta \sqrt{S_{ij,t} m_{ij}^*} \end{cases} \tag{9}$$

where Y_{ij}^*, R_{ij}^*, G_{ij}^*, β, $S_{ij,n}$, $S_{ij,t}$, and m_{ij}^* all are a function of the material's properties. The relations between these parameters

Table 3 Values of the parameters used in the simulations

Parameters	Values
Wall density, ρ_w	7800 kg m^{-3}
Young's modulus of walls, Y_w	200 GPa
Restitution coefficient of particles, ε_p	0.7
Restitution coefficient of walls, ε_w	0.9
Poison ratio of particles, ν_p	0.3
Poison ratio of walls, ν_w	0.27

and the material's properties are given by eqn (10)

$$\begin{cases} \frac{1}{Y_{ij}^*} = \frac{\left(1-\nu_i^2\right)}{Y_i} + \frac{\left(1-\nu_j^2\right)}{Y_j} \\ \frac{1}{G_{ij}^*} = \frac{2(2-\nu_i)(1+\nu_i)}{Y_i} + \frac{2(2-\nu_j)(1+\nu_j)}{Y_j} \\ S_{ij,n} = 2 Y_{ij}^* \sqrt{R_{ij}^* \delta_{n_{ij}}} \\ S_{ij,t} = 2 G_{ij}^* \sqrt{R_{ij}^* \delta_{t_{ij}}} \\ \beta = \frac{\ln \varepsilon}{\sqrt{\ln^2(\varepsilon) + \pi^2}} \end{cases} \tag{10}$$

where Y is the Young's modulus, G is the shear modulus, ν is the Poisson ratio, and ε is the coefficient of restitution. The effective R_{ij}^* and m_{ij}^* can be calculated from the radii and masses of the particles in contact:

$$\begin{cases} \frac{1}{R_{ij}^*} = \frac{1}{R_i} + \frac{1}{R_j} \\ \frac{1}{m_{ij}^*} = \frac{1}{m_i} + \frac{1}{m_j} \end{cases} \tag{11}$$

Table 3 lists the physical parameters adopted in the simulations.

The Rayleigh and Hertz times, Δt_r and Δt_h, defined in eqn (12) are taken as the estimates of the binary contact time.

$$\begin{aligned} \Delta t_r &= \pi R \sqrt{\frac{\rho}{G}} \Big/ (0.1631\nu + 0.8766) \\ \Delta t_h &= 2.87\left(m^{*2}/R^* \cdot Y^{*2} \cdot V_{max}\right)^{0.2} \end{aligned} \tag{12}$$

In eqn (12) V_{max} is the maximum relative velocity of two particles in contact. The Rayleigh time Δt_r is calculated for each particle in the simulation. The Hertz time Δt_h is estimated by testing a collision of each particle with itself using V_{max} as the assumed collision velocity. Throughout the simulations, the specified time step remains less than 1% of the minimum value of Δt_r and Δt_h.

We performed constant *NVE* integration based on the velocity-Verlet integration scheme to update the position, velocity, and angular velocity for finite-size spherical particles.

The directional constant torque model is applied as a rolling resistance model, which exerts a constant torque on a particle to represent the rolling friction. The direction of the torque is always against the relative rotation between the two contacting entities. The torque is applied in pairs on each pair of particles

 This journal is © The Royal Society of Chemistry 2020

Published on 18 December 2019. Downloaded on 2/14/2020 10:45:36 AM.

in contact. In the 2D case, the torque between two in contact disks i and j can be expressed as

$$M_r = -\frac{\omega_{rel}}{|\omega_{rel}|}\mu_r R_r F_n \tag{13}$$

$$\omega_{rel} = \omega_i - \omega_j \tag{14}$$

where ω_i and ω_j are the angular velocities of disks i and j respectively and ω_{rel} is the relative angular velocity between them.

Appendix B: Theoretical model for the proportionate growth of the instability pattern

In this section, we endeavor to account for the proportionate growth mode dominating the growth of the stable instability pattern based on the continuum model. We assume that the granular flows are incompressible, implying that the packing fraction remains constant in the limit of dense close packing inside the compaction front.

Fig. 18(a) presents the sketches of the cross-sectional and top views of the particles in the neighborhood of the compaction front. The dynamics of the newly compacted particles are dictated by force balance:

$$P_{comp} - P_{collision} - 2f_{p\text{-}w} = \rho_0 \mu_p v_{comp} \tag{15}$$

where u_p is the particle velocity just in the wake of the compaction front, ρ_0 is the initial mass density, *i.e.*, $\rho_0 = \phi_0\rho_p$, v_{comp} is the propagating velocity of the compaction front, P_{comp} and $P_{collision}$ are the outward and inward pressure exerted on particles which are about to be encompassed by the compaction front, respectively, $P_{comp} \gg P_{collision}$, and $f_{p\text{-}w}$ is the mobilized friction force per unit surface exerted on compacted particles by the top (bottom) plate. The circular compaction front indicates homogeneous u_p and v_{comp} independent of the azimuthal angles. Thus P_{comp} is independent of the azimuthal angles.

For the incompressible granular flows inside the compaction front, the constitutive law of the steady flows takes the form of a visco-plastic law, in which the stress tensor is given by

$$\sigma_{ij} = -P_p\delta_{ij} + \tau_{ij} \tag{16}$$

where P_p is the isotropic pressure inside the particles,

$$\tau_{ij} = \eta\dot{\gamma}_{ij}, \quad \eta = \frac{\mu(I)P_p}{|\dot{\gamma}|} \tag{17}$$

where $|\dot{\gamma}|$ is the second invariant of the shear rate tensor: $|\dot{\gamma}| = \sqrt{1/2\dot{\gamma}_{ij}\dot{\gamma}_{ij}}$. The viscosity η depends on the shear rate, the pressure, and the effective friction coefficient μ, which is a function of the dimensionless inertial number

$$I = \frac{|\dot{\gamma}|d_p}{\sqrt{P_p/\rho_p}} \tag{18}$$

The function $\mu(I)$ can be fitted as follows

$$\mu(I) = \mu_1 + \frac{\mu_2 - \mu_1}{I_0/I + 1} \tag{19}$$

Assuming that the spatial variation of the steady divergent flow mainly takes place in the radial direction rather than the azimuthal or vertical directions, the mass and radial momentum conversation equations reduce to

$$\frac{\partial(\rho_{comp} r v_r)}{\partial r} = 0 \tag{20}$$

$$\rho_{comp} v_r \frac{\partial v_r}{\partial r} = -\frac{\partial P_p}{\partial r} + \left(\frac{1}{r}\frac{\partial(r\tau_{rr})}{\partial r} - \frac{\tau_{\theta\theta}}{r}\right) \tag{21}$$

For the radially divergent incompressible flows where the plane strain condition is assumed, if the inner surface $r = R_0$ expands at a uniform velocity V_0, the strain rate tensor [d] and

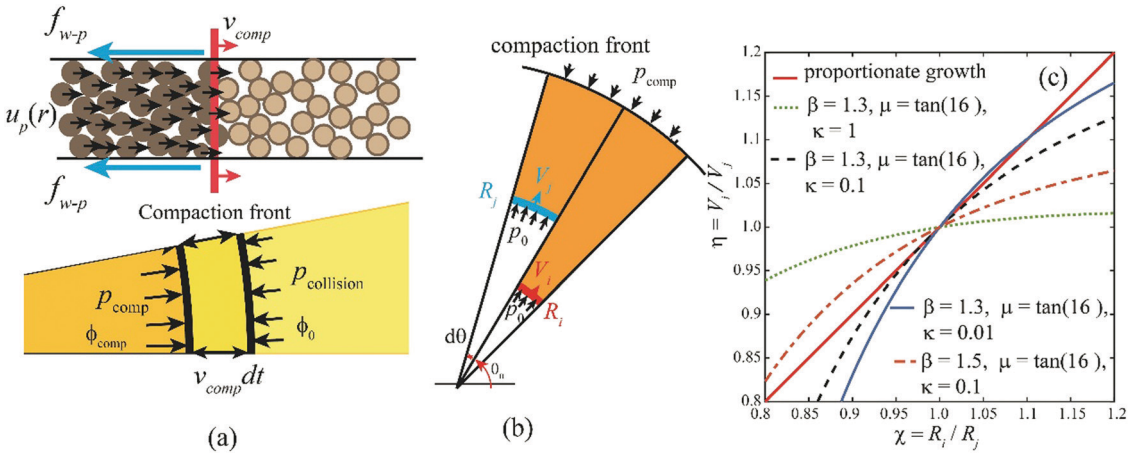

Fig. 18 (a) Schematic side view (top panel) and top view (bottom panel) of areas across the compaction front. (b) Schematic representation of the radial channel geometry if the annular compaction band is to be divided into a series of radially aligned channels. The interface between the particles and gas is located at R_i in channel 'i' and at R_i in channel 'j'. The two channels experience an identical pressure drop over the distance from the interfaces to the compaction front. (c) Variations of $\eta = V_i/V_j$ with $\chi = R_i/R_j$ predicted by eqn (29).

Published on 18 December 2019. Downloaded on 2/14/2020 10:45:36 AM.

the corresponding shear rate are

$$[\mathrm{d}] = \begin{bmatrix} -\frac{R_0 V_0}{r^2} & 0 & 0 \\ 0 & \frac{R_0 V_0}{r^2} & 0 \\ 0 & 0 & 0 \end{bmatrix} \tag{22}$$

$$\dot{\gamma}_{rr} = -\frac{R_0 V_0}{r^2}, \quad \dot{\gamma}_{\theta\theta} = \frac{R_0 V_0}{r^2}, \quad |\dot{\gamma}| = \frac{R_0 V_0}{r^2} \tag{23}$$

Substituting eqn (23) into eqn (17) leads to

$$\tau_{rr} = -\mu(I) P_\mathrm{p}, \quad \tau_{\theta\theta} = \mu(I) P_\mathrm{p} \tag{24}$$

Since $V_0 \sim 10^1$ m s^{-1} derived from Fig. 6(a) and (b), $R_0 \sim 10^{-1}$ m, the shear rate $|\dot{\gamma}| \sim 10^2$ s^{-1}, $P_\mathrm{p} \sim 10^5$ Pa, $d_\mathrm{p} \sim 10^{-5}$ m, and $\rho_\mathrm{p} \sim 10^3$ kg m^{-3}, the inertial number I is estimated on the order of O(10^{-4}–10^{-3}). Small values of I correspond to a quasi-static regime in the sense that macroscopic deformation is slow compared to microscopic rearrangement. $\mu(I)$ converges to μ_1 when I approaches zero according to eqn (19).

The continuity condition (eqn (20)) leads to

$$v_r = \frac{R_0 V_0}{r}. \tag{25}$$

By substitution of eqn (24) and (25) into eqn (21), the momentum equation becomes

$$[1 + \mu(I)]\frac{\partial P_\mathrm{p}}{\partial r} + 2\mu(I)\frac{P}{r} = \rho_\mathrm{comp}\frac{(R_0 V_0)^2}{r^3} \tag{26}$$

The analytical solution of eqn (26) is given by

$$P_\mathrm{p} = \left(\Delta p_0 + \frac{\rho_\mathrm{comp} V_0^2}{2}\right) \cdot \left(\frac{R_0}{r}\right)^{\xi} - \frac{\rho_\mathrm{comp} V_0^2}{2}\left(\frac{R_0}{r}\right)^2 \quad \text{with} \quad \xi = \frac{2\mu(I)}{1+\mu(I)} \tag{27}$$

where $\xi = 2\mu_1/(1 + \mu_1)$ when I approaches zero.

If the annular compact band is to be divided into a large number of wedge-like channels as shown in Fig. 18(b), the pressures at the compaction front for all channels are identical, $P_\mathrm{p}(r = R_\mathrm{comp}) = P_\mathrm{comp}$. Considering two neighboring channels with inner radii of R_i and R_j, respectively, as shown in Fig. 18(b), the interface velocities at the respective channels are $v_r\,(r = R_i) = V_i$, and $v_r\,(r = R_j) = V_j$. The pressure being equalized in these two channels at $r = R_\mathrm{comp}$ leads to

$$\left(\Delta p_0 + \frac{\rho_\mathrm{comp} V_i^2}{2}\right)\cdot\left(\frac{R_i}{R_\mathrm{comp}}\right)^{\xi} - \frac{\rho_\mathrm{comp} V_i^2}{2}\left(\frac{R_i}{R_\mathrm{comp}}\right)^2 = \left(\Delta p_0 + \frac{\rho_\mathrm{comp} V_j^2}{2}\right)\cdot\left(\frac{R_j}{R_\mathrm{comp}}\right)^{\xi} - \frac{\rho_\mathrm{comp} V_j^2}{2}\left(\frac{R_j}{R_\mathrm{comp}}\right)^2 \tag{28}$$

If we assume $\Delta p_0 = \kappa \cdot \rho_\mathrm{comp} V_j^2/2$ where $\kappa \in (0,1)$, $\chi = R_i/R_j$ and $\beta = R_\mathrm{comp}/R_i$ where χ varies in the range of $1/\beta$ to β, $\beta > 1$. The ratio between V_i and V_j, $\eta = V_i/V_j$, becomes a function of χ, β, κ, and μ.

$$\eta = \frac{V_i}{V_j} = \sqrt{\frac{\left[(\kappa+1)\cdot\left(\frac{1}{\chi\beta}\right)^{\xi} - \left(\frac{1}{\chi\beta}\right)^2\right]}{\left[(\kappa+1)\cdot\left(\frac{1}{\beta}\right)^{\xi} - \left(\frac{1}{\beta}\right)^2\right]}} \tag{29}$$

Since the local rheology employed here is calibrated against monodisperse spherical particles, we apply the above continuum model to the systems of spherical glass beads and PMMA spheres. As deduced from Fig. 6, $\beta_\mathrm{glass} \sim 1.3$, and $\beta_\mathrm{PMMA} \sim 1.5$, and using the inter-particle friction to estimate μ, $\mu_\mathrm{glass} \sim \tan(16^\circ)$, and $\mu_\mathrm{PMMA} \sim \tan(16^\circ)$, we plot the variations of η with χ derived from eqn (29) as shown in Fig. 18(c). Alongside the expansion of the particle ring, the internal interfacial pressure quickly decays, thus three curves of $\eta(\chi)$ with $\kappa = 1$, 0.1, and 0.01 are depicted in Fig. 16(c) to demonstrate the effect of Δp_0.

The proportional growth demands η scale with χ with unit proportionality as denoted by the red line in Fig. 18(c). The deviation between the curve $\eta(\chi)$ and the line $\eta = \chi$ is indicative of the likelihood of the proportionate growth being maintained. The growth mode increasingly deviates from proportionate growth with the increase of disturbances, namely as χ moves away from unity, which justifies the fact that only small instabilities are sustained in the stable glass bead and PMMA sphere patterns governed by the proportionate growth. Also disturbances seem not to survive during the early times when the interfacial pressure Δp_0 is still high.

References

1 D. L. Frost, *Shock Waves*, 2018, **28**, 439–449.
2 Y. Formenti, T. H. Druitt and K. Kelfoun, *Bull. Volcanol*, 2003, **65**, 587–605.
3 T. Inoue, R. Yamazaki and S.-I. Inutsuka, *Astrophys. J.*, 2009, **695**, 825–833.
4 Y. Aglitskiy, A. L. Velikovich, M. Karasik, N. Metzler, S. T. Zalesak, A. J. Schmitt, L. Phillips, J. H. Gardner, V. Serlin, J. L. Weaver and S. P. Obenschain, *Philos. Trans. R. Soc., A*, 2010, **368**, 1739–1768.
5 R. K. Eckhoff, *Int. J. Chem. Eng.*, 2009, **2009**, 569825.
6 L. F. David, G. Yann, P. Oren, G. Samuel and Z. Fan, *Phys. Fluids*, 2012, **24**, 091109.
7 Y. Gregoire, D. Frost and O. Petel, *AIP Conf. Proc.*, 2012, **1426**, 1623–1626.
8 D. L. Frost, J. Loiseau, B. J. Marr and S. Goroshin, *AIP Conf. Proc.*, 2017, **1793**, 120020.
9 J. Loiseau, Q. Pontalier, A. M. Milne, S. Goroshin and D. L. Frost, *Shock Waves*, 2018, **28**, 473–487.
10 K. Xue, F. Li and C. Bai, *Eur. Phys. J. E: Soft Matter Biol. Phys.*, 2013, **36**, 1–16.
11 K. Xue, K. Du, X. Shi, Y. Gan and C. Bai, *Soft Matter*, 2018, **14**, 4422–4431.
12 V. Rodriguez, R. Saurel, G. Jourdan and L. Houas, *Phys. Rev. E: Stat., Nonlinear, Soft Matter Phys.*, 2013, **88**, 063011.

 This journal is © The Royal Society of Chemistry 2020

Published on 18 December 2019. Downloaded on 2/14/2020 10:45:36 AM.

13 V. Rodriguez, R. Saurel, G. Jourdan and L. Houas, *Shock Waves*, 2017, **27**, 187–198.
14 K. Kandan, S. N. Khaderi, H. N. G. Wadley and V. S. Deshpande, *J. Mech. Phys. Solids*, 2017, **109**, 217–240.
15 S. Ukai, K. Balakrishnan and S. Menon, *Phys. Fluids*, 2010, **22**, 104103.
16 K. Balakrishnan, *Phys. Fluids*, 2014, **26**, 043303.
17 J. C. Schulz, K. C. Gottiparthi and S. Menon, *Phys. Fluids*, 2013, **25**, 114105.
18 B. Meng, J. Zeng, B. Tian, L. Li, Z. He and X. Guo, *Phys. Fluids*, 2019, **31**, 074102.
19 A. Milne, C. Parrish and I. Worland, *Shock Waves*, 2010, **20**, 41–51.
20 A. M. Milne, E. Floyd, A. W. Longbottom and P. Taylor, *Shock Waves*, 2014, **24**, 501–513.
21 J. Y. Huang, L. Lu, D. Fan, T. Sun, K. Fezzaa, S. L. Xu, M. H. Zhu and S. N. Luo, *Scr. Mater.*, 2016, **111**, 114–118.
22 R. S. Crum, M. A. Homel, D. C. Pagan, E. B. Herbold, D. Miller, J. Lind, B. J. Jensen, A. J. Iverson and M. C. Akin, *J. Appl. Phys.*, 2019, **125**, 025902.
23 H. Mo, F.-S. Lien, F. Zhang and D. S. Cronin, *Shock Waves*, 2018, **28**, 559–577.
24 H. Mo, F.-S. Lien, F. Zhang and D. S. Cronin, *J. Appl. Phys.*, 2019, **125**, 214302.
25 Ø. Johnsen, R. Toussaint, K. J. Måløy and E. G. Flekkøy, *Phys. Rev. E: Stat., Nonlinear, Soft Matter Phys.*, 2006, **74**, 011301.
26 J. L. Vinningland, Ø. Johnsen, E. G. Flekkøy, R. Toussaint and K. J. Måløy, *Phys. Rev. Lett.*, 2007, **99**, 048001.
27 X. Cheng, L. Xu, A. Patterson, H. M. Jaeger and S. R. Nagel, *Nat. Phys.*, 2008, **4**, 234.
28 J. M. Campbell, D. Ozturk and B. Sandnes, *Phys. Rev. Appl.*, 2017, **8**, 064029.
29 F. K. Eriksen, R. Toussaint, A. L. Turquet, K. J. Måløy and E. G. Flekkøy, *Phys. Rev. E*, 2018, **97**, 012908.
30 T. S. Majmudar and R. P. Behringer, *Nature*, 2005, **435**, 1079.
31 A. H. Clark, L. Kondic and R. P. Behringer, *Phys. Rev. Lett.*, 2012, **109**, 238302.
32 A. H. Clark, A. J. Petersen, L. Kondic and R. P. Behringer, *Phys. Rev. Lett.*, 2015, **114**, 144502.
33 Y. Yang, Y. M. Cheng and Q. C. Sun, *Powder Technol.*, 2017, **318**, 528–542.
34 P. Guo and X. Su, *Can. Geotech. J.*, 2007, **44**, 579–591.
35 R. Freeman, *Powder Technol.*, 2007, **174**, 25–33.
36 C. G. Christoph Kloss, A. Hager, S. Amberger and S. Pirker, *Prog. Comput. Fluid Dyn.*, 2012, **12**, 140–152.
37 H. P. Zhu, Z. Y. Zhou, R. Y. Yang and A. B. Yu, *Chem. Eng. Sci.*, 2007, **62**, 3378–3396.
38 Y. J. Huang, C. K. Chan and P. Zamankhan, *Phys. Rev. E: Stat., Nonlinear, Soft Matter Phys.*, 2010, **82**, 031307.
39 J. Ai, J.-F. Chen, J. M. Rotter and J. Y. Ooi, *Powder Technol.*, 2011, **206**, 269–282.
40 J. P. Joy, S. N. Pathak, D. Das and R. Rajesh, *Phys. Rev. E*, 2017, **96**, 032908.
41 K. Xue, L. Sun and C. Bai, *Phys. Rev. E*, 2016, **94**, 022903.
42 K. Xue, H. Cui, K. Du, X. Shi, Y. Gan and C. Bai, *Powder Technol.*, 2018, **336**, 220–229.
43 I. Bischofberger, R. Ramachandran and S. R. Nagel, *Soft Matter*, 2015, **11**, 7428–7432.
44 I. Bischofberger and S. R. Nagel, *Phys. Today*, 2016, **69**, 70–71.
45 Y. Forterre and O. Pouliquen, *Ann. Rev. Fluid Mech*, 2008, **40**, 1–24.
46 A. Alsiny, I. Vardoulakis and A. Drescher, *Geotechnique*, 1992, **42**, 395–410.
47 C. W. MacMinn, E. R. Dufresne and J. S. Wettlaufer, *Phys. Rev. X*, 2015, **5**, 011020.
48 A. Britan and G. Ben-Dor, *Int. J. Multiphase Flow*, 2006, **32**, 623–642.
49 C. H. Rycroft, *Chaos*, 2009, **19**, 041111.